Food Hydrocolloids 184 (2027) 113247

Contents lists available at ScienceDirect

Food Hydrocolloids

journal homepage: www.elsevier.com/locate/foodhyd

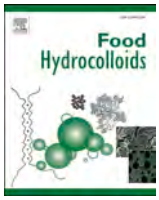

From seaweed biorefinery residues to functional films: how H_2O_2/UV-assisted pigment removal reshapes polymer networks and material performance

Hylenne Bojorges [a], Yubexi Correa [c], Marta Martínez-Sanz [c], Amparo López-Rubio [a,b], María José Fabra [a,b,*]

[a] Food Safety and Preservation Department, IATA-CSIC, Avda. Agustín Escardino 7, Paterna, Valencia, 46980, Spain
[b] Interdisciplinary Platform for Sustainable Plastics Towards a Circular Economy-Spanish National Research Council (SusPlast-CSIC), Madrid, Spain
[c] Instituto de Investigación en Ciencias de la Alimentación, CIAL (CSIC-UAM, CEI UAM + CSIC), Nicolás Cabrera, 9, Madrid, 28049, Spain

ARTICLE INFO

Keywords:
Seaweed biorefinery residues
Polysaccharide-protein interactions
Food packaging

ABSTRACT

Seaweed biorefinery residues are often regarded as cellulose-rich side streams; however, their conversion into functional films depends on how extraction and post-treatment steps preserve the residual polymer matrix. This study evaluated H_2O_2/UV-assisted pigment removal as both an optical-upgrading strategy and a matrix-modifying treatment for residue-based films. Solid residues remaining after furcellaran extraction from *Furcellaria lumbricalis*, alginate extraction from *Saccharina latissima*, and protein extraction from *Ulva lactuca* were processed by extrusion and hot pressing before and after pigment removal. The materials were characterized through compositional, spectroscopic, morphological, scattering, thermal, optical, mechanical, water-affinity, and barrier analyses. All untreated residues formed self-supporting films, but performance was strongly residue-specific. *Furcellaria lumbricalis* residues yielded the most cohesive films, with the highest tensile strength (8.0 ± 0.5 MPa), lowest water vapor permeability (2.4 ± 0.1 × 10^{-13} kg m·Pa^{-1}·s^{-1}·m^{-2}), low water uptake (12.1 ± 1.2%), and effective light shielding. *Saccharina latissima* residues produced more extensible but weaker films, whereas *Ulva lactuca* films showed higher water affinity and permeability. Pigment removal improved whiteness, but its functional impact depended on matrix architecture. Treated *Saccharina latissima* failed to form a continuous film, while treated *Ulva lactuca* showed the highest permeability and water uptake. These findings indicate that H_2O_2/UV-assisted pigment removal should not be regarded only as an optical treatment, since its impact depends strongly on the organization and composition of the residual polymer matrix: when cohesive protein-polysaccharide domains were preserved, film integrity and water resistance were maintained; when these domains were depleted, processability and barrier performance deteriorated. The results provide a structure-function basis for selecting seaweed biorefinery residues as sustainable film-forming matrices with packaging-relevant functionality.

1. Introduction

Sustainable films derived from renewable biopolymers have attracted increasing attention as potential alternatives to conventional food-packaging materials due to their biodegradability and tunable functional properties (Díaz-Montes, 2022). Among these materials, macroalgae represent a promising source of structurally diverse polysaccharides, including sulfated galactans, alginates, ulvans, and cellulose-rich assemblies, which can contribute to film formation, moisture regulation, light protection, and mechanical stability (Thiviya et al., 2023).

Seaweed biorefinery processes generate substantial solid residues after extracting high-value compounds such as furcellaran, alginate, and proteins. These residues are often considered low-value side streams, despite retaining complex polymeric matrices that may contribute to film formation and packaging-relevant functionality. Unlike purified polysaccharides, seaweed biorefinery residues contain interacting fractions of cellulose, non-cellulosic polysaccharides, proteins, minerals,

* Corresponding author. Food Safety and Preservation Department, IATA-CSIC, Avda. Agustín Escardino 7, Paterna, 46980, Valencia, Spain
E-mail addresses: hylenne@iata.csic.es (H. Bojorges), mjfabra@iata.csic.es (M.J. Fabra).

https://doi.org/10.1016/j.foodhyd.2026.113247
Received 27 May 2026; Received in revised form 27 July 2026; Accepted 11 August 2026
Available online 14 August 2026

and minor compounds (Bojorges et al., 2022). This compositional complexity may be advantageous because residual proteins and amorphous polysaccharide fractions can contribute to matrix continuity, flexibility, and moisture-barrier behavior through protein-polysaccharide and polysaccharide-polysaccharide interactions (Athanasopoulou et al., 2024; Bealer et al., 2020).

Although seaweed-derived polysaccharides have been widely explored as film-forming materials, studies using minimally processed seaweed biorefinery residues remain comparatively limited. In these residues, the unresolved question is not whether hydrocolloid networks affect film properties, which is already well recognized, but how prior extraction and post-treatment steps alter the residual polymer architecture that supports film formation. This distinction is particularly relevant for packaging-oriented films, where mechanical resistance, moisture sensitivity, and light-barrier properties may depend not only on cellulose-rich ordered domains, but also on retained non-cellulosic polysaccharides, proteins, minerals, and minor hydrophobic fractions. In minimally processed seaweed residues, however, how H_2O_2/UV-assisted pigment removal alters this balance and its consequences for film formation remain insufficiently understood.

For packaging-oriented film development, the intense coloration of seaweed residues is not a minor aesthetic issue, as it may affect visual compatibility with packaged foods, consumer perception, and the optical performance of the final material (Steiner & Florack, 2023). Therefore, pigment removal is a relevant strategy for broadening the use of seaweed residues as film-forming matrices. However, in complex biorefinery residues, pigments are not isolated components; they coexist with proteins, sulfated polysaccharides, uronic-acid-rich domains, minerals, and soluble amorphous fractions that may contribute to matrix cohesion (Krishnan et al., 2024). Consequently, oxidative pigment-removal treatments may improve optical appearance while also modifying structural components of the residual matrix (Chang et al., 2023; Yao et al., 2023).

In this context, the study was designed around three contrasting residual matrices: furcellaran-extracted *Furcellaria lumbricalis*, alginate-extracted *Saccharina latissima*, and protein-extracted *Ulva lactuca*. These materials were not purified polysaccharides, but residue-specific polymer architectures shaped by both macroalgal origin and prior extraction history. Their response to H_2O_2/UV-assisted pigment removal was therefore expected to depend on whether the treatment preserved or disrupted the domains responsible for matrix cohesion.

Based on this rationale, this study examined H_2O_2/UV-assisted pigment removal as an optical-upgrading strategy for seaweed biorefinery residues, with particular attention to its impact on the matrix cohesion required for film formation. Untreated and pigment-removed residues were processed by extrusion and hot pressing to evaluate the effects of treatment on residue-specific matrix organization, water interactions, barrier behavior, and packaging-relevant functionality.

2. Materials and methods

2.1. Materials and reagents

The seaweeds *Saccharina latissima* and *Ulva lactuca* were kindly provided by Porto-Muiños S. L. (Cerceda, A Coruña, Spain) in the form of dry powders. The industrial solid residue from *Furcellaria lumbricalis* was supplied by Seaweesh (Tallinn, Estonia) as a dry powder. According to the supplier-provided manufacturing documentation, this residue was generated during industrial furcellaran production from dried, stored, washed, weighed, and extracted seaweed; after extraction, the liquor was separated from the remaining seaweed solids. The residue was supplied as a dry powder, and no additional chemical treatment of the separated residue stream was indicated in the information provided by the supplier. Proprietary extraction parameters, including extraction temperature, extraction time, and solid-to-liquid ratio, were not disclosed.

Alginate extraction from *S. latissima* was conducted following the procedure described by Bojorges et al. (2022). Briefly, after alginate recovery, the remaining insoluble fraction was collected, freeze-dried, and used as a film-forming residue. The protein-extracted residue from *U. lactuca* was obtained using a pH-shift extraction process, as previously reported by Vega-Gómez et al. (2024). The insoluble fraction remaining after protein extraction was freeze-dried and used for film preparation. Unless otherwise stated, all residues were stored under dry conditions until further processing.

2.2. Compositional analysis seaweed residues

The protein content was determined from total nitrogen content using an Elemental Analyzer Rapid N Exceed (Paralab S.L., Spain), applying a nitrogen to protein conversion factor of 5.0 (Angell et al., 2016).

Carbohydrate content and monosaccharide composition were determined according to the methodology described by Bojorges et al. (2023). Monosaccharides were quantified using high-performance anion-exchange chromatography coupled with pulsed amperometric detection (HPAEC-PAD, Switzerland). Calibration was performed using analytical standards of fucose, mannitol, rhamnose, arabinose, xylose, galactose, glucose, 6-O-metilgalactose, 3,6-anhydrogalactose, galacturonic acid, glucuronic acid, iduronic acid, mannuronic acid, and guluronic acid. Commercial ulvan and microcrystalline cellulose were also used as reference controls.

The lipid and ash content were determined, according to the AOAC Official Methods 991.36 and 920.153, respectively AOAC (1990). All analyses were carried out in triplicate.

2.3. H_2O_2/UV-assisted pigment removal

The residues were subjected to an H_2O_2/UV-assisted pigment-removal treatment following the methodology described by Freitas et al. (2024), with slight modifications. Briefly, the samples were treated with 4% (w/v) H_2O_2 at a solid-to-liquid ratio of 1:20 (g/mL) in glass Petri dishes to ensure uniform contact between the solid residue and the treatment medium. Since the pH of the suspensions ranged between 9.0 and 9.5, no external buffering agent was added. Magnesium sulfate ($MgSO_4$, 0.1%, w/w) was incorporated to stabilize the reaction.

The mixtures were exposed to ultraviolet (UV) irradiation for 4 h, maintaining a distance of 3 cm between the UV lamp and the sample surface. During treatment, the suspensions were stirred every 20 min to promote homogeneous exposure to the pigment-removal medium. After treatment, the residues were washed with distilled water until neutral pH and freeze-dried prior to further use. The untreated residues from *F. lumbricalis*, *S. latissima*, and *U. lactuca* were coded as FR, SR, and UR, respectively. After H_2O_2/UV-assisted pigment removal, the corresponding treated residues were coded as DF, DS, and DU, respectively.

2.4. Production of algal residue-based films

Algal residue-based films were produced by extruding mixtures of seaweed residue powder with glycerol as a plasticizer at 30% (w/w) relative to the total solid content. This glycerol concentration and the extrusion conditions were selected based on previously reported seaweed residue-based formulations processed under comparable thermomechanical conditions (Hernández-García et al., 2026; Sanz et al., 2026). The mixtures were processed using an Xplore Micro Compounder 15HT (Sittard, The Netherlands) at 130 °C and 100 rpm for 4 min.

For film formation, 3 g of the extruded material was uniformly distributed onto Teflon sheets and subjected to a three-step compression-molding process using a hydraulic hot-plate press (Model LP20, Labtech Engineering, Thailand). The first cycle was conducted at 160 °C under 30 bar for 3 min, followed by a second cycle at 160 °C under

150 bar for an additional 3 min. The final cycle involved cooling to below 80 °C while maintaining 150 bar for 3 min. The same extrusion and compression-molding conditions were applied to all formulations to evaluate the film-forming response of the different residual matrices under comparable processing conditions.

Films were coded by adding "-Film" to the corresponding residue code. Thus, FR-Film, SR-Film, UR-Film, DF-Film, and DU-Film refer to films prepared from FR, SR, UR, DF, and DU residues, respectively. No DS-Film was obtained because DS did not form a continuous film under the processing conditions used. Prior to characterization, all film specimens were conditioned at 53% RH and 22 °C for one week using a saturated magnesium nitrate solution. Unless otherwise stated, the same conditioning protocol was applied before optical, structural, thermal, mechanical, surface, water uptake, and water vapor permeability analyses.

2.5. Physical characterization

2.5.1. Thickness

Film thickness was measured using a digital micrometer (Model ATO-JZ0-25, Spain) with a resolution of 0.001 mm. Measurements were taken at six randomly selected positions on each film specimen.

2.5.2. Moisture content

The moisture content of the conditioned films was determined gravimetrically in accordance with ASTM D644-99 (ASTM, 2007). Film specimens were weighed, oven-dried at 105 °C for 24 h, and weighed again. Moisture content was calculated from the weight loss after drying and expressed as a percentage of the dry film weight.

2.5.3. Antioxidant-related properties

The antioxidant-related properties of the untreated and pigment-removed residues and their corresponding films were evaluated through ABTS radical scavenging capacity and total phenolic content. For the ABTS assay, aqueous extracts were prepared from each sample at a concentration of 5 mg/mL. The assay was performed following the Trolox equivalent antioxidant capacity method described by Re et al. (1999), with minor modifications. Briefly, 20 μL of each sample extract was mixed with 230 μL of $ABTS^{\bullet+}$ working solution, and the absorbance was measured at 734 nm after 6 min of reaction. Trolox was used as the calibration standard, and the results were expressed as μmol Trolox equivalents (TE)/g dry sample. All measurements were performed in triplicate.

Total phenolic content was determined using the Folin-Ciocalteu assay, adapted from Singleton et al. (1999). For this analysis, 0.2 mL of sample extract (5 mg/mL) was mixed with 1 mL of Folin-Ciocalteu reagent previously diluted 1:10 with distilled water. Subsequently, 0.8 mL of Na_2CO_3 solution (75 mg/mL) was added, and the mixture was incubated at 50 °C for 30 min. The absorbance was then recorded at 750 nm. Gallic acid was used to construct the calibration curve, and the results were expressed as mg gallic acid equivalents (GAE)/g dry sample. Analyses were carried out in triplicate.

2.6. Structural and morphological characterization

2.6.1. Scanning Electron Microscopy (SEM)

Film morphology was analyzed using a Hitachi S-4800 scanning electron microscope operated at 10 kV and a working distance of 8-12 mm. Film cross-sections were obtained after cryo-fracturing the samples in liquid nitrogen. The fractured specimens were mounted on aluminum holders and sputter-coated with a gold-palladium layer under vacuum prior to imaging.

2.6.2. Fourier transform infrared spectroscopy (FTIR)

FTIR spectra of dry residue powders and conditioned film specimens were recorded using a Bruker Vertex spectrometer equipped with an attenuated total reflectance (ATR) accessory. Spectra were collected over the wavenumber range 4000-400 cm^{-1} at a resolution of 4 cm^{-1}, with 64 accumulated scans per sample. Spectra were baseline-corrected and normalized before comparison. The 1800-1500 cm^{-1} region was additionally inspected to evaluate treatment-induced changes associated with carbonyl, amide, and carboxylate-containing groups.

2.6.3. Small-angle and wide-angle X-ray scattering (SAXS/WAXS)

Combined SAXS/WAXS experiments were carried out in the Non-Crystalline Diffraction beamline, BL-11, at ALBA synchrotron light source (www.albasynchrotron.es). The seaweed residues and small pieces of the films were placed into 2 mm quartz capillaries (Hilgenberg GmbH, Germany) and sealed before being analyzed. The energy of the incident photons was 12.4 keV or equivalently a wavelength, λ, of 1 Å. The SAXS scattering patterns were collected by means of a photon counting detector, Pilatus 1M, with an active area of 168.7 × 179.4 mm^2, an effective pixel size of 172 × 172 μm^2 and a dynamic range of 20 bits. The sample-to-detector distance was set to 6700 mm, resulting in a q range with a maximum value of q = 0.2 $Å^{-1}$. Additionally, the WAXS diffraction patterns were collected by means of a 3 CCD detector Rayonix LX255-HS with an active area of 85 × 255 mm^2, an effective pixel size of 44 × 44 μm^2 and a dynamic range of 16 bits. In this case, the sample-to-detector distance was set to 105 mm, corresponding to a maximum q value of 7.87 $Å^{-1}$. This detector was tilted with a pitch of 26.4°. An exposure time of 15 s was selected to obtain sufficient signal while avoiding detector saturation. Data reduction was treated by pyFAI python code (ESRF) (Kieffer & Wright, 2013), modified by ALBA beamline staff, to do on-line azimuthal integrations from a previously calibrated file. The calibration files were created from a silver behenate (AgBh) standard. The intensity profiles were then represented as a function of q using the IRENA macro suite (Ilavsky & Jemian, 2009) within the Igor software package (Wavemetrics, Lake Oswego, Oregon).

WAXS peak fitting was performed in Igor, following the procedure described in a previous work (Martínez-Sanz et al., 2018). The obtained values from the fitting coefficients were those that minimized the value of Chi-squared, which is defined as:

$$x^2 = \sum \left(\frac{y - y_i}{\sigma_i} \right)^2 \quad (1)$$

where y represents the fitted value for a given point, y_i corresponds to the value of the measured data for that point and σ_i is an estimate of the standard deviation for y_i.

The curve fitting operation was carried out iteratively and, at each iteration, the fitting coefficients were refined to minimize x^2. From the fitting results obtained, the apparent crystallinity index was determined by applying Eq. (2):

$$X_C(\%) = \frac{\Sigma A_{Crystal}}{A_{Total}} \times 100 \quad (2)$$

where A_{Total} represents the sum of the areas under all diffraction peaks and $\Sigma A_{Crystal}$ corresponds to the sum of the areas corresponding to the crystalline peaks.

2.7. Optical and surface properties

2.7.1. Optical properties

Film transparency was evaluated from surface reflectance spectra using a CM-26D spectrophotometer (Konica Minolta, Japan) with an illuminated area diameter of 10 mm. Three specimens from each film were analyzed against white and black backgrounds. Transparency (Ti) was calculated according to the Kubelka-Munk theory for multiple scattering, using the reflectance of the sample layer over a known white background and an ideal black background, as described by (Fabra et al., 2009). Transparency values ranged theoretically from 0 to 100.

The colorimetric properties of both seaweed residues and films were determined to minimize the influence of film porosity on optical measurements. Color parameters were measured using a CR-400 colorimeter (Konica Minolta, Japan) and expressed as lightness (L*), chroma (C^*_{ab}), and hue (h^*_{ab}). The whiteness index (WI) was calculated using Eq. (3). Measurements were performed in triplicate, with three readings per replicate.

$$WI = 100 - \sqrt{(100 - L^*)^2 + a^{*2} + b^{*2}} \quad (3)$$

2.7.2. Water contact angle measurement

The surface wettability of algal residue-based films was evaluated using a DSA25 goniometer (Krüss, Germany) equipped with AD4021 image analysis software under ambient conditions. A ~3 μL droplet of distilled water was deposited onto the film surface, and the contact angle was determined after 10 s by image analysis of the droplet profile. At least six measurements were performed for each film formulation.

2.8. Mechanical and thermal properties

2.8.1. Mechanical properties

The tensile strength (TS), elastic modulus (E), and elongation at break (ϵb) of the films were evaluated using a universal testing machine (Instron, USA) according to ASTM standard method D882.10 (ASTM, 2001). Tensile parameters were obtained from stress-strain curves generated from force-displacement data using film specimens measuring 1 cm × 8 cm. Prior to testing, the films were conditioned at 53 ± 2% relative humidity and 22 ± 2 °C. Film thickness was measured before testing and used to calculate the cross-sectional area of each specimen. The specimens were mounted in pneumatic film grips and stretched at a crosshead speed of 50 mm min^{-1} until rupture. At least six replicates were analyzed for each film formulation.

2.8.2. Thermal properties

Thermogravimetric analysis (TGA) was performed to evaluate the thermal stability of the seaweed residues using a TA 550 analyzer (Waters-TA Instruments, USA). Approximately 5 mg of each sample was heated from 30 to 700 °C at 10 °C/min under a nitrogen atmosphere. The derivative thermogravimetric (DTG) curves were obtained from the first derivative of the weight-loss profiles as a function of temperature.

The thermal behavior of the films was further analyzed by differential scanning calorimetry (DSC) using a TA Instruments thermal analysis system (New Castle, DE, USA) under a nitrogen atmosphere. Approximately 3 mg of each sample was analyzed from 20 to 200 °C at a heating rate of 10 °C min^{-1}. The DSC instrument was calibrated using indium as a reference standard, and baseline correction was performed using an empty pan. All analyses were conducted in triplicate.

2.9. Permeability and sorption properties

2.9.1. Water vapor permeability (WVP)

Water vapor permeability was determined gravimetrically at 23 °C according to the ASTM method (ASTM, 2010) by monitoring weight gain over time. Film samples were analyzed in triplicate under a relative humidity gradient of 0–75%.

The films were mounted between the upper and lower sections of Payne permeability cups (3.5 cm diameter; Elcometer SPRL, Belgium), with silica gel placed inside the lower chamber. A Viton rubber O-ring was positioned between the film and the cell to ensure an airtight seal. The assembled permeability cells were stored in a controlled-humidity chamber maintained at 75% relative humidity using a saturated sodium chloride solution. WVP was calculated from the steady-state weight gain, exposed film area, water vapor pressure difference, and measured film thickness.

2.9.2. Water uptake

The water absorption properties of the films were assessed by measuring their weight gain over time. Before testing, the samples were dried at 60 °C until reaching a constant weight. They were then placed in a humidity-controlled chamber maintained at 75% relative humidity using a saturated sodium chloride solution. Gravimetric measurements were conducted until the samples reached a stable weight. At least three replicates were analyzed for each film formulation. Water uptake was expressed as the percentage of weight gain relative to the initial dry weight of the films.

2.10. Statistical analysis

Statistical analyses were performed using SPSS software (IBM Corp., USA). One-way analysis of variance (ANOVA) followed by Tukey's post hoc test was used to determine significant differences among samples at the $p < 0.05$ significance level.

3. Results and discussion

3.1. Chemical composition of untreated and pigment-removed seaweed residues

The chemical composition of the untreated and pigment-removed residues was analyzed to define the initial composition of the residual polymer matrices (Table 1). Carbohydrates were the main component of the untreated residues, ranging from 39.8 ± 3.2% in FR to 48.5 ± 2.8% in UR, followed by proteins and ash. FR and SR showed high protein contents of 38.4 ± 0.1% and 39.3 ± 0.2%, respectively, whereas UR contained a markedly lower protein fraction (17.3 ± 0.5%) and the highest ash content among the untreated residues (27.2 ± 3.4%). These differences reflect both the intrinsic biochemical diversity of red, brown, and green macroalgae and the selective nature of the previous extraction processes used to obtain each residual matrix (Bojorges et al., 2022; Uranga et al., 2023). In particular, the low protein content of UR is consistent with its origin as the insoluble fraction remaining after targeted protein extraction.

The monosaccharide profiles further evidenced the residue-specific composition of the remaining polymer matrices. FR contained 9.7 ± 1.8 g/100 g dry basis of 3,6-anhydrogalactose, together with glucose and 6-O-methyl-galactose, indicating the presence of residual furcellaran-like galactan domains after extraction. SR was characterized by alginate-associated uronic acids, including GulA, GlcA, and ManA at 2.2 ± 0.2, 2.0 ± 0.1, and 2.1 ± 0.1 g/100 g dry basis, respectively, as well as fucose (2.7 ± 0.1 g/100 g dry basis), consistent with residual alginate- and fucoidan-associated structures. In contrast, UR showed higher levels of rhamnose, xylose, GlcA, and iduronic acid, with values of 6.9 ± 0.6, 5.1 ± 0.4, 3.2 ± 0.2, and 5.5 ± 0.4 g/100 g on a dry basis, respectively, consistent with the presence of ulvan-type polysaccharides. These compositional fingerprints indicate that each residue retained a distinct polymeric matrix, with different proportions of cellulose-associated structural domains and non-cellulosic polysaccharide fractions.

Once the composition of the untreated residues was established, the effect of H_2O_2/UV-assisted pigment removal was evaluated to determine how this treatment modified the residual matrices. The treatment induced marked compositional changes, although their extent varied among residues. Solid yields after treatment ranged from 36.9 ± 3.9% for DS to 51.7 ± 4.2% for DF, indicating different susceptibilities of the matrices to the treatment medium. Protein content decreased in all treated residues, with the most pronounced reduction observed in *S. latissima*, from 39.3 ± 0.2% in SR to 16.3 ± 0.1% in DS. Smaller decreases were observed in *F. lumbricalis* and *U. lactuca*, from 38.4 ± 0.1% to 35.5 ± 0.1% and from 17.3 ± 0.5% to 16.4 ± 0.4%, respectively. These changes are consistent with the susceptibility of proteinaceous components to oxidative degradation under peroxide-based treatments

Table 1
Chemical composition of untreated and pigment-removed seaweed biorefinery residues.

Composition (dry wt. %)	Untreated seaweed residues			Pigment-removed seaweed residues		
	F. lumbricalis (FR)	*S. latissima* (SR)	*U. lactuca* (UR)	*F. lumbricalis* (DF)	*S. latissima* (DS)	*U. lactuca* (DU)
Yield (%)	*n.a.*	*n.a.*	*n.a.*	51.7 ± 4.2^{c}	36.9 ± 3.9^{a}	45.8 ± 5.1^{b}
Protein	38.4 ± 0.1^{c}	39.3 ± 0.2^{c}	17.3 ± 0.5^{a}	35.5 ± 0.1^{b}	16.3 ± 0.1^{a}	16.4 ± 0.4^{a}
Ash	19.3 ± 0.7^{ab}	12.6 ± 0.2^{a}	27.2 ± 3.4^{bc}	25.2 ± 2.3^{bc}	26.8 ± 2.5^{bc}	29.9 ± 1.4^{c}
Lipids	3.1 ± 0.6^{b}	<0.5	2.4 ± 0.3^{b}	0.7 ± 0.2^{a}	<0.5	0.8 ± 0.2^{a}
Carbohydrates[a]	39.8 ± 3.2^{b}	43.6 ± 3.6^{b}	48.5 ± 2.8^{b}	30.8 ± 1.8^{a}	44.5 ± 2.0^{b}	39.5 ± 2.2^{b}
of which (g/100 g dry basis)						
Fucose	*n.d.*	2.7 ± 0.1^{b}	*n.d.*	*n.d.*	0.6 ± 0.1^{a}	*n.d.*
Galactose	2.3 ± 1.4^{b}	0.5 ± 0.1^{a}	4.0 ± 0.7^{c}	1.5 ± 0.4^{ab}	0.2 ± 0.0^{a}	1.6 ± 0.5^{ab}
Cellulose[b]	21.7 ± 3.3^{a}	29.4 ± 5.6^{bc}	15.9 ± 0.6^{a}	23.0 ± 1.3^{ab}	35.9 ± 4.6^{c}	20.3 ± 2.7^{a}
Glucose[c]	2.6 ± 0.1^{b}	3.1 ± 0.1^{c}	5.4 ± 0.2^{d}	0.5 ± 0.1^{a}	2.8 ± 0.2^{b}	5.1 ± 0.2^{d}
Xylose	*<0.5*	1.0 ± 0.1^{a}	5.1 ± 0.4^{c}	*n.d.*	1.2 ± 0.1^{a}	3.4 ± 0.6^{b}
GalA	*n.d.*	*n.d.*	2.5 ± 0.3^{b}	*n.d.*	*n.d.*	0.5 ± 0.2^{a}
Rhamnose	*<0.5*	*n.d.*	6.9 ± 0.6^{b}	*<0.5*	*n.d.*	3.9 ± 0.3^{a}
GulA	*n.d.*	2.2 ± 0.2^{b}	*n.d.*	*n.d.*	0.7 ± 0.1^{a}	*n.d.*
GlcA	*n.d.*	2.0 ± 0.1^{b}	3.2 ± 0.2^{c}	*n.d.*	1.0 ± 0.2^{a}	1.5 ± 0.2^{a}
ManA	*n.d.*	2.1 ± 0.1^{b}	*n.d.*	*n.d.*	0.5 ± 0.1^{a}	*n.d.*
Iduronic acid	*n.d.*	*n.d.*	5.5 ± 0.4^{b}	*n.d.*	*n.d.*	3.2 ± 0.5^{a}
Mannitol	*n.d.*	0.6 ± 0.1^{a}	*n.d.*	*n.d.*	1.6 ± 0.3^{b}	*n.d.*
6-O-Me-Gal	1.1 ± 0.4^{a}	*n.d.*	*n.d.*	1.4 ± 0.2^{a}	*n.d.*	*n.d.*
3,6-AnGal	9.7 ± 1.8^{b}	*n.d.*	*n.d.*	4.4 ± 0.5^{a}	*n.d.*	*n.d.*

Values are expressed as means ± SD (n = 3). Different letters within the same row indicate significant differences ($p < 0.05$). n.a., not applicable; n.d., not detected; <0.5, below the reporting limit. GulA, GlcA, ManA, and GalA denote guluronic, glucuronic, mannuronic, and galacturonic acids, respectively.

[a] Total carbohydrate content calculated as the sum of all monosaccharides detected by HPAEC-PAD.

[b] The crystalline cellulose content was quantified as the difference between the Saeman sulfuric hydrolysis method (Saeman, 1945) and the non-crystalline glucose content obtained through acid methanolysis (Bertaud et al., 2002; Willför et al., 2009).

[c] Glucose contribution from the non-crystalline fraction.

(Davies, 2016), suggesting partial solubilization or degradation of fractions that may contribute to matrix cohesion through protein-polysaccharide interactions. Lipid removal was also observed in FR and UR, with values decreasing from 3.1 ± 0.6% to 0.7 ± 0.2% in *F. lumbricalis* and from 2.4 ± 0.3% to 0.8 ± 0.2% in *U. lactuca*, indicating that pigment removal also affected minor hydrophobic fractions within the residual matrix.

Beyond the changes observed in proteins and lipids, the carbohydrate fraction provided further evidence that pigment removal modified the residual polymer matrix. In *S. latissima*, total carbohydrate content remained high after pigment removal, and cellulose showed a numerically higher value in DS than in SR (35.9 ± 4.6% and 29.4 ± 5.6%, respectively). Although this difference was not statistically significant (Table 1), it was accompanied by a marked decrease in uronic acids, indicating a compositional shift toward a relatively cellulose-rich residual matrix with partial removal of alginate-associated domains. This shift was reflected in the reduction of GulA, GlcA, and ManA from 2.2 ± 0.2, 2.0 ± 0.1, and 2.1 ± 0.1 g/100 g dry basis in SR to 0.7 ± 0.1, 1.0 ± 0.2, and 0.5 ± 0.1 g/100 g dry basis in DS, respectively. In *F. lumbricalis*, pigment removal decreased total carbohydrates from 39.8 ± 3.2% in FR to 30.8 ± 1.8% in DF and reduced 3,6-anhydrogalactose from 9.7 ± 1.8 to 4.4 ± 0.5 g/100 g dry basis, indicating partial loss of furcellaran-related galactan domains. In *U. lactuca*, total carbohydrate content decreased numerically from 48.5 ± 2.8% in UR to 39.5 ± 2.2% in DU. At the same time, ulvan-related monosaccharides were reduced, including rhamnose, GalA, GlcA, and iduronic acid, which decreased from 6.9 ± 0.6, 2.5 ± 0.3, 3.2 ± 0.2, and 5.5 ± 0.4 g/100 g dry basis in UR to 3.9 ± 0.3, 0.5 ± 0.2, 1.5 ± 0.2, and 3.2 ± 0.5 g/100 g dry basis in DU, respectively. Similar reductions in non-cellulosic polysaccharide fractions have been reported for hydrogen-peroxide-assisted treatments applied to lignocellulosic residues (Freitas et al., 2024; Tareen et al., 2020). The treatment, therefore, produced residue-dependent compositional shifts extending beyond pigment removal, involving protein-rich, lipidic, and non-cellulosic polysaccharide fractions.

3.2. Structural characterization by FTIR

FTIR spectroscopy was used to examine the compositional and structural changes associated with pigment removal. Representative spectra of the untreated and pigment-removed residues are shown in Fig. 1. The spectra of the untreated residues displayed features characteristic of complex polysaccharide–protein matrices. After pigment removal, the broad O–H/N–H stretching band between 3600 and 3000 cm^{-1} became sharper and more defined, particularly in DS. This narrowing suggests changes in the hydrogen-bonding environment and a lower contribution of amorphous or protein-associated fractions, consistent with the compositional changes observed after treatment. Similar sharpening of hydroxyl-related bands has been associated with a more defined hydrogen-bonding environment in cellulose-rich fractions (Freitas et al., 2022).

To further evaluate whether the H_2O_2/UV-assisted pigment-removal treatment produced spectroscopically detectable oxidative

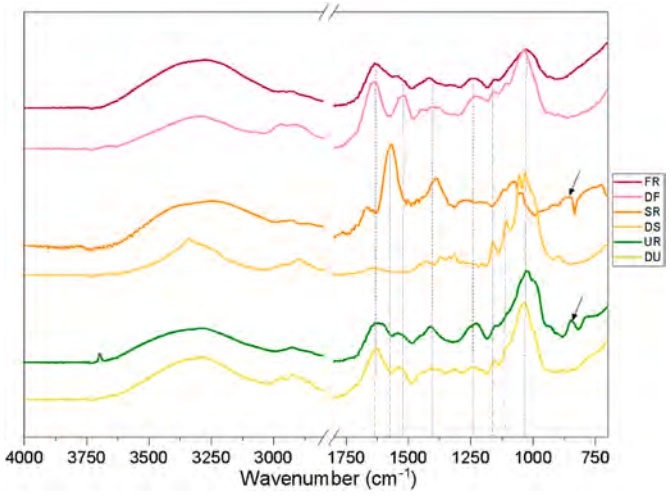

Fig. 1. FTIR spectra of untreated and pigment-removed seaweed residues.

modifications, the 1800–1500 cm^{-1} region was examined in detail. This region includes the carbonyl range, where aldehyde- or other carbonyl-containing groups may contribute, but also contains overlapping signals from Amide I, carboxylate groups, and bound water. No distinct new band was observed around 1720-1740 cm^{-1} in the pigment-removed residues, indicating that ATR-FTIR did not show clear evidence of aldehyde- or carbonyl-group accumulation under the conditions used. Instead, the most relevant treatment-induced changes were concentrated in the 1650-1600 cm^{-1} region and near 1540 cm^{-1}, pointing mainly to modifications in protein- and uronic-acid-associated domains.

Consistent with this interpretation, the overlapping Amide I/carboxylate region around 1650-1600 cm^{-1} and the Amide II region near ~1540 cm^{-1}, which were more evident in the untreated residues, decreased in intensity after the pigment-removal treatment. This attenuation was especially clear in DS and was consistent with the reduction in protein content shown in Table 1. Rather than indicating complete protein removal, these changes suggest a reduced contribution of proteinaceous components in the treated residues, likely due to partial oxidation, solubilization, or removal during washing. Similar effects have been reported for peroxide-based treatments applied to

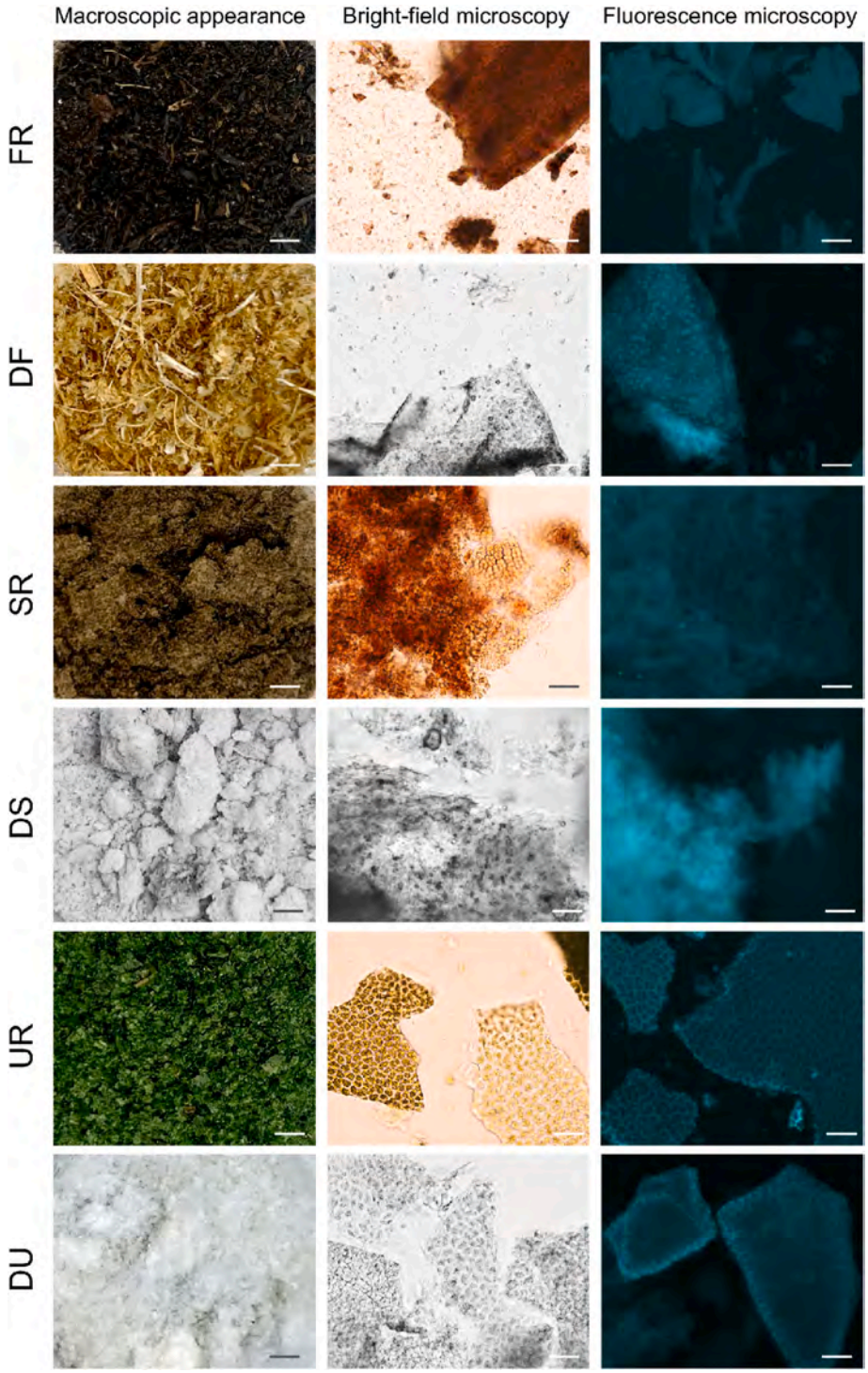

Fig. 2. Macroscopic and microscopic characterization of untreated and pigment-removed residues. Representative images show the visual appearance, bright-field microscopy, and fluorescence microscopy of each sample. Scale bars correspond to 2 mm for macroscopic images and 100 μm for microscopy images.

lignocellulosic and protein-containing matrices (Davies, 2016; Dutra et al., 2018).

The attenuation of amide-related bands was accompanied by changes in the fingerprint region, where signals associated with non-cellulosic polysaccharides became less prominent. Bands around ~1410 cm^{-1}, associated with C-OH bending and symmetric stretching of carboxylate groups, and ~1220 cm^{-1}, assigned to S=O stretching of sulfated polysaccharides, decreased after pigment removal (Blanco-Pascual et al., 2014; Bojorges et al., 2022). This decrease is consistent with the partial removal of uronate and sulfate-containing polysaccharides, including alginate, fucoidan, and ulvan-related fractions. In contrast, the band near ~1034 cm^{-1}, attributed to C-O-C stretching vibrations of glycosidic linkages, remained present in all samples, indicating that the main polysaccharide backbone of the residual matrix was not extensively disrupted (Salem & Ismail, 2022). The reduction of the C-O-S vibration around ~850 cm^{-1} in *S. latissima* and *U. lactuca* further supported the lower contribution of sulfated groups after treatment (Yaich et al., 2017).

The magnitude of these spectral changes was strongly residue-dependent, indicating that pigment removal reshaped each residual matrix according to its initial polymer composition rather than acting as a uniform purification step. The most evident modification occurred in *S. latissima*, whose treated residue showed a clearer separation of polysaccharide-related bands after pigment removal. This behavior was consistent with the strong reduction in protein and uronic acid content observed for DS in Table 1. By contrast, *F. lumbricalis* and *U. lactuca* retained broader spectral profiles, consistent with a more heterogeneous contribution of residual furcellaran and ulvan related fractions. These spectral features point to residue-specific matrix modification, primarily involving proteinaceous and non-cellulosic polysaccharide fractions, with no distinct ATR-FTIR signature of aldehyde accumulation.

3.3. Visual appearance and morphological characterization

Optical microscopy was used to evaluate how pigment-removal treatment affected the visual appearance and microscopic organization of seaweed residues. Representative images are shown in Fig. 2, together with the macroscopic appearance of the untreated and pigment-removed samples.

The macroscopic images showed a clear change in residue color after pigment-removal treatment, although the extent of this change differed among species. This trend was supported by the color coordinates and whiteness index (WI) reported in Table 2. Untreated residues showed low L* and WI values, particularly FR, which presented the lowest L* and WI values (10.0 ± 1.3 and 10.0 ± 1.2, respectively), reflecting the intense coloration of the original biorefinery side streams. After treatment, L* and WI increased in all cases, with the highest values observed for DU, followed by DS and DF.

Among the treated residues, DU displayed the greatest whitening effect, reaching the highest L* and WI values. DS also showed a substantial increase in lightness and whiteness, although its final color remained less bright than DU's. In contrast, DF retained a more yellowish appearance, with lower WI and higher chroma than the other pigment-removed residues. This response suggests lower pigment-removal efficiency in *F. lumbricalis*, possibly due to a stronger association of colored compounds with residual polysaccharide-protein structures. Polyphenolic compounds in algae may interact with cell-wall polysaccharides and proteins through non-covalent and, in some cases, covalent associations, thereby reducing their extractability or oxidative susceptibility (Besednova et al., 2020). In this context, the comparatively high residual protein content of DF after treatment (Table 1), together with its broader FTIR profile, is consistent with the persistence of protein-associated colored fractions.

Table 2
Color coordinates and whiteness index (WI) of untreated and pigment-removed seaweed residues.

Color properties				
Sample	L*	C*	h°	*WI*
FR	10.0 ± 1.3^{a}	2.9 ± 0.8^{a}	62.7 ± 1.5^{a}	10.0 ± 1.2^{a}
SR	30.7 ± 1.5^{c}	13.1 ± 1.4^{b}	74.8 ± 1.9^{b}	29.4 ± 0.9^{c}
UR	17.1 ± 1.4^{b}	12.5 ± 0.8^{b}	118.0 ± 0.5^{d}	16.2 ± 1.3^{b}
DF	48.1 ± 1.3^{d}	24.0 ± 1.4^{d}	77.6 ± 1.5^{b}	42.8 ± 1.4^{d}
DS	70.9 ± 1.1^{e}	17.7 ± 0.7^{c}	89.6 ± 2.2^{c}	67.1 ± 1.1^{e}
DU	90.5 ± 1.4^{f}	17.5 ± 0.5^{c}	88.9 ± 0.5^{c}	80.0 ± 0.6^{f}

Values are expressed as means ± SD (n = 3). Different letters within the same column indicate significant differences ($p < 0.05$).

Optical microscopy revealed marked differences in the organization of the untreated residues. FR and SR displayed larger and more defined cell-wall fragments, whereas UR showed thinner and more dispersed structures. These differences are consistent with the taxonomic origin of the residues and with the distinct polymeric architectures described in the compositional analysis. After pigment-removal treatment, the main cell-wall outlines remained visible in most samples, indicating that the treatment did not fully disrupt the residual morphology at the microscopic scale. Nevertheless, the extent of structural preservation was residue dependent.

The most evident morphological change occurred in SR after treatment. DS showed less compact cellular aggregates, with individual cell wall fragments appearing more widely separated than in the untreated residue. This separation is consistent with the compositional decrease in protein and uronic acid content (Table 1) and with the attenuation of protein- and sulfate-associated FTIR bands. Proteins and glycoproteins can contribute to cell-wall cohesion by mediating interactions between cellulose and matrix polysaccharides through hydrogen bonding, electrostatic interactions, and other non-covalent associations (Fuertes-Rabanal et al., 2025; Gordalina et al., 2021). Their partial removal could therefore contribute to weaker intercellular adhesion and greater separation of cell-wall fragments (Kloareg et al., 2021; O'Brien et al., 2022).

In the case of *S. latissima*, the concurrent reduction of alginate-associated components may have further reduced the continuity of the non-cellulosic matrix. Alginate plays an important structural role in brown algal cell walls, where it can interact with cellulose microfibrils and divalent cations, particularly Ca^{2+}, contributing to matrix organization and mechanical stability (Bojorges et al., 2022; Terauchi et al., 2016). The partial removal of alginate-rich domains during pigment-removal treatment would therefore be expected to reduce the continuity of the non-cellulosic matrix. Polyphenolic compounds, including phlorotannins in brown algae, may also participate in extracellular matrix stabilization through interactions with proteins and polysaccharides (Gómez & Huovinen, 2020; Imbs & Zvyagintseva, 2018). The microscopy results, therefore, support the compositional and FTIR evidence that pigment removal modified not only the color of the residues but also the organization of matrix components involved in cell-wall cohesion.

3.4. Thermal stability of untreated and pigment-removed residues

The thermal stability of the untreated and pigment-removed residues was evaluated by thermogravimetric analysis (TGA). The corresponding derivative thermogravimetric (DTG) curves, shown in Fig. 3, revealed residue-dependent degradation patterns that reflected differences in the compositions of the residual matrices and their prior extraction histories. The pigment-removal treatment modified these profiles, although the direction and extent of the changes depended on the initial residue composition.

The untreated residues of *S. latissima* and *U. lactuca* showed broad degradation profiles, consistent with their multicomponent composition. In SR, an initial shoulder between 130 and 150 °C was observed, which may be associated with the release of retained moisture and the

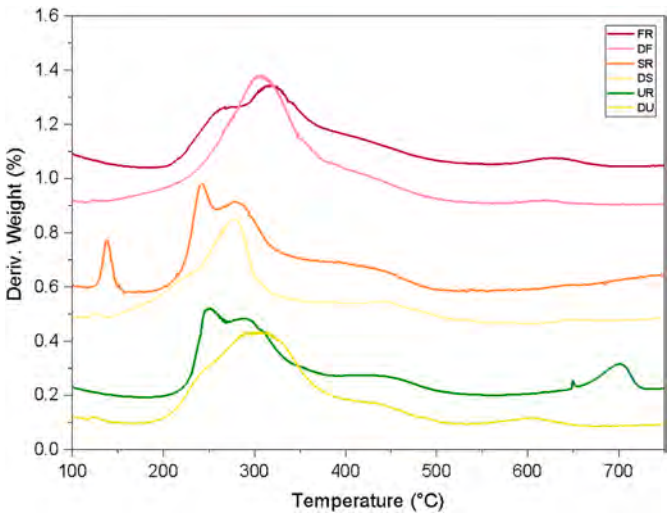

Fig. 3. Derived thermogravimetric curves (DTG) of untreated and pigment-removed residues.

degradation of low-molecular-weight compounds (Ross et al., 2009). Both SR and UR displayed overlapping degradation events, with a first contribution around 250 °C and a second one near 280 °C. These events can be associated with the overlapping thermal decomposition of non-cellulosic polysaccharides, such as alginate-rich fractions in *S. latissima* and ulvan-related domains in *U. lactuca*, as well as the contribution of cellulose-rich fractions at higher temperatures (Martínez-Sanz et al., 2020).

A distinct thermal response was observed for FR, which showed a shoulder around 280 °C, followed by a main degradation event near 300 °C. This behavior is consistent with the presence of residual furcellaran-like galactans associated with the cellulose-rich fraction. Sulfated galactans can form networks stabilized by hydrogen bonding and cation-mediated interactions, which may contribute to a denser matrix and delay thermal degradation (Eha et al., 2017; Petcharat et al., 2025). In UR, a minor high-temperature event was also detected, likely associated with inorganic salts or carbonized residues left over from earlier degradation steps, in agreement with the high ash content of this residue (Alboofetileh et al., 2025).

After pigment-removal treatment, the main degradation events of DF and DU shifted toward approximately 300 °C, indicating changes in the thermal response of these residues. This shift may be related to the partial retention of furcellaran and ulvan-related polysaccharides within the remaining residual matrix. Although the specific interactions cannot be resolved from TGA alone, previous solid-state NMR studies have shown that matrix polysaccharides can interact with cellulose surfaces and influence local molecular mobility (Wang et al., 2020; Wang & Hong, 2016). Such associations could reduce the thermal accessibility of cellulose-rich domains, contributing to the slightly higher apparent degradation temperature observed for DF and DU.

The behavior of DS differed from that of DF and DU. Despite showing the highest cellulose content after treatment (Table 1), DS exhibited a lower main degradation temperature, around 280 °C. This result is consistent with the extensive removal of alginate- and fucoidan-associated components during pigment-removal treatment, which may have left a more exposed cellulose-rich structure. The reduction of surrounding matrix polysaccharides could increase the accessibility of cellulose-rich domains to thermal degradation. This behavior reinforces the interpretation that thermal stability was governed by the organization of the residual matrix rather than by cellulose content alone.

3.5. Structural and physicochemical characterization of the films

After characterizing the untreated and pigment-removed residues, their ability to form continuous films was evaluated by extrusion followed by hot pressing. This processing approach was selected to assess the intrinsic film-forming capacity of each residue without further purification or incorporation of external film-forming polymers. The resulting materials were then analyzed to determine how the initial residue composition and the changes induced by pigment-removal treatment influenced their structural organization and functional properties.

3.5.1. Optical properties and microstructure of the films

Fig. 4a shows the visual appearance of the films obtained from untreated and pigment-removed residues. Most formulations produced self-supporting films, although all samples exhibited an opaque, colored appearance after thermomechanical processing. This coloration was evident even in films prepared from pigment-removed residues, suggesting that optical appearance was not only determined by the initial pigment content of the residues. Processing temperatures during extrusion and hot pressing may have favored thermally induced reactions involving residual proteins, carbohydrates, and oxidizable phenolic compounds, contributing to brownish or reddish tones in the final films. Similar color development has been reported in thermally processed biopolymeric systems, where Maillard-type reactions or non-enzymatic oxidation products can be generated during heating (Freitas et al., 2024; Plaza et al., 2010).

A relevant difference was observed for the pigment-removed *S. latissima* residue, which did not form a cohesive film under the processing conditions used. This behavior is consistent with the compositional changes described above, particularly the marked reduction in proteins and uronic-acid-rich polysaccharides after pigment-removal treatment. In brown algal residues, alginate-rich fractions and residual proteins can contribute to matrix continuity through polysaccharide-polysaccharide and protein-polysaccharide interactions (Bojorges, López-Rubio et al., 2025; Pereira et al., 2021). Their partial removal may therefore reduce the number of cohesive domains available to bind cellulose-rich structures during thermomechanical processing. Although DS showed the highest cellulose content among the pigment-removed residues, this enrichment was not sufficient to preserve film formation, suggesting that processability in these residue-based matrices depended on more than cellulose content alone (Klonos et al., 2022).

In contrast, residues from *F. lumbricalis* and *U. lactuca* formed continuous films both before and after pigment-removal treatment. This behavior suggests that these residues retained enough non-cellulosic polysaccharides and protein-associated fractions to maintain matrix continuity during processing. In DF and DU, these remaining components may have provided interfacial cohesion between cellulose-rich domains and the surrounding amorphous matrix, allowing film formation despite the compositional losses induced by pigment-removal treatment.

Consistent with their visual opacity, the internal transmittance spectra shown in Fig. 4b revealed limited light transmission across most of the visible region. FR-Film, SR-Film, and UR-Film showed very low Ti values across the blue-green region, generally remaining close to or below 2% up to 660 nm. The pigment-removal treatment increased internal transmittance mainly in DF-Film and DU-Film, particularly toward the red region of the spectrum. At 600 nm, Ti increased from 0.43% in FR-Film to 7.54% in DF-Film and from 1.25% in UR-Film to 14.70% in DU-Film. Film transparency is strongly influenced by the internal organization of the matrix, since heterogeneous structures promote light scattering and reduce light transmission (Pérez-Bassart et al., 2023). In the present films, the combination of residual pigments, thermally generated colored compounds, and microstructural heterogeneity likely contributed to the pronounced opacity. From a packaging-oriented perspective, this low transmittance may be

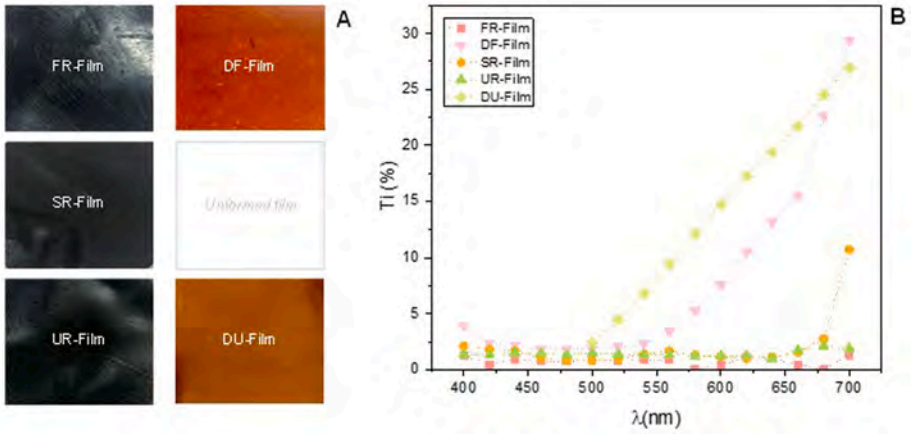

Fig. 4. (a) Visual appearance and (b) spectral distribution of their internal transmittance and (Ti) of films produced from untreated and pigment-removed residues.

beneficial for materials intended to reduce light exposure, particularly for products susceptible to photoinduced oxidation.

The persistence of absorption at lower wavelengths may be related to residual colored species or to compounds formed during thermomechanical processing. Polyphenols, quinone-type oxidation products, and melanoidin-like structures are known to absorb in the visible region and contribute to brownish coloration in biopolymer matrices (Singh et al., 2022; Xiao et al., 2020). Antioxidant-related properties were evaluated in both residues and films to assess the presence of phenolic or radical-scavenging compounds before and after pigment-removal treatment and thermomechanical processing (Supplementary Material, Tables S1 and S2). Pigment removal markedly reduced the antioxidant-related properties of the residues (Table S1). However, measurable Folin-Ciocalteu and ABTS responses were still detected in several films (Table S2), including those prepared from pigment-removed residues. Because thermomechanical processing may promote the formation and/or increase the extractability of reducing compounds that also react in these assays (Amarowicz, 2009; Pastoriza & Rufián-Henares, 2014), these responses should not be interpreted as direct evidence of retained native polyphenols or as proof of antioxidant active-packaging functionality. Therefore, the residual coloration observed in the films cannot be attributed solely to native phenolic compounds but is also consistent with the formation of thermally generated chromophores during processing. Such compounds may develop conjugated structures that give rise to yellow, brown, or reddish hues (Bruhns et al., 2019; Starowicz & Zieliński, 2019). These observations indicate that the optical response of the films was governed not only by the initial pigment content of the residues but also by processing-induced chemical changes and matrix heterogeneity.

To further relate the films' optical response to their internal organization, SEM cross-sectional images were analyzed (Fig. 5). Film microstructure varied according to the residual matrix used for processing, reflecting both macroalgal origin and prior extraction history. Differences among films prepared from untreated residues were more evident than the morphological changes induced by the pigment-removal treatment, suggesting that the initial matrix composition played a dominant role at the SEM observation scale.

Films derived from *F. lumbricalis* residues showed comparatively compact and homogeneous cross-sections. This morphology is consistent with the combined presence of residual proteins and furcellaran-related polysaccharide fractions in FR and DF (Table 1), which may favor interactions with polysaccharide fractions and contribute to matrix cohesion. Protein-polysaccharide interactions, including hydrogen bonding and electrostatic associations, are known to support continuous structures in biopolymer films (Calva-Estrada et al., 2019; Karakuş, 2025). In this case, the denser appearance of FR- and DF-based films

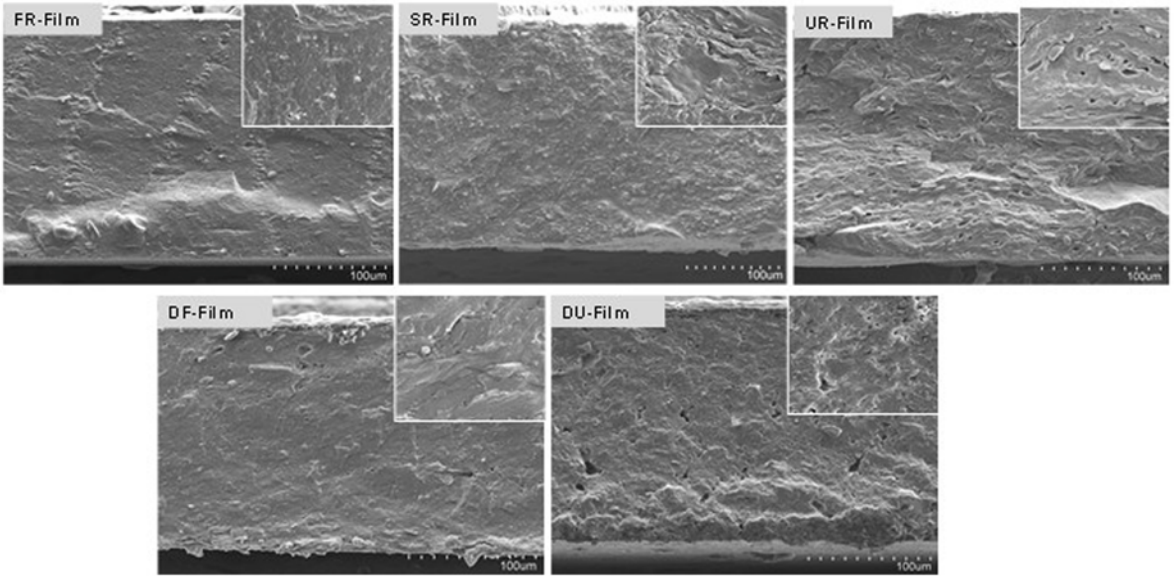

Fig. 5. SEM cross-sectional images of films produced from untreated and pigment-removed residues.

suggests good embedding of cellulose-associated domains within a cohesive residual polymer matrix.

Films prepared from *U. lactuca* residues showed a more irregular cross-sectional morphology, with visible discontinuities and microvoids. This behavior may be related to the lower protein content of UR and DU (Table 1), as well as to higher contribution of ulvan-related polysaccharides and mineral components. A reduced fraction of interfacial proteinaceous material may limit the cohesion between polysaccharide-rich and fibrous domains, favoring a less compact structure. Similar effects have been described in biopolymer composites where insufficient interfacial adhesion promotes structural defects and weakens matrix continuity (Aaliya et al., 2021; Khan et al., 2025). The SR-Film showed an intermediate morphology, with a relatively continuous cross-section but greater surface irregularity than the *F. lumbricalis* films, consistent with a matrix that retained film-forming ability but displayed lower structural compactness.

The effect of pigment-removal treatment on film morphology was less evident than its effect on residue composition. In DF- and DU-Films, cellulose-rich domains appeared embedded within the surrounding matrix, without forming clearly separated fibrous regions at the scale analyzed. The absence of major morphological rearrangements suggests that extrusion and hot pressing promoted partial integration of the residual components, even when the pigment-removal treatment had altered the composition of the starting residues. The preservation of a continuous microstructure in DF- and DU-Films contrasts with the behavior of DS, where the stronger loss of protein- and uronic-acid-rich fractions was associated with the absence of a self-supporting film under the same processing conditions.

3.5.2. *Structural characterization of the films*

FTIR spectroscopy was used to evaluate the effects of thermomechanical processing on the molecular features of the residue-based films. Fig. 6 shows the spectra of the residues (dashed lines) and their corresponding films (solid lines), allowing direct comparison. The main bands associated with macroalgal polysaccharides and residual proteins remained evident after film formation. However, changes in band intensity and definition were observed, consistent with residue-dependent rearrangements in intermolecular organization after extrusion, hot pressing, and glycerol plasticization.

All films exhibited a broad absorption band around 3300 cm^{-1}, associated with O–H stretching vibrations. Compared with the raw residues, this band tended to become more intense and defined in the films, indicating alterations in the hydrogen-bonding environment during thermomechanical processing. The Amide I (~1624 cm^{-1}) and Amide II (1540 cm^{-1}) bands, attributable to protein backbone vibrations (Bojorges, Martínez-Sanz, et al., 2025), consistently appeared with lower intensity in the films, suggesting partial denaturation or reorganization of residual proteins under the applied processing conditions.

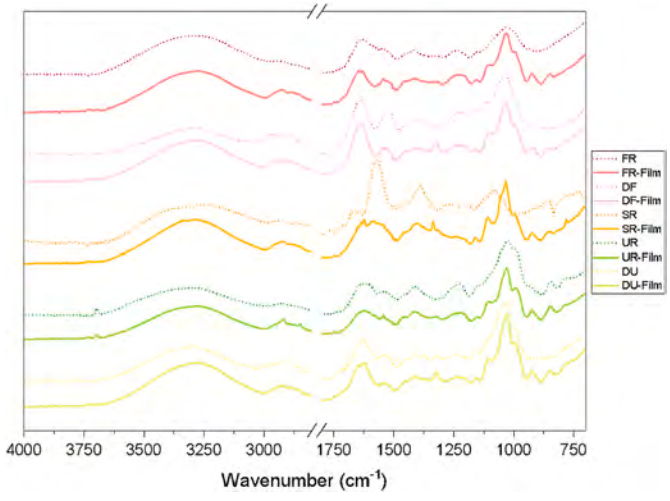

Fig. 6. FTIR spectra of residues, represented by dashed lines, and their corresponding films, represented by solid lines, obtained from untreated and pigment-removed seaweed residues.

Changes associated with sulfated polysaccharides were also observed. The characteristic sulfate ester band at ~1240 cm^{-1}, previously assigned to sulfated polysaccharides in macroalgal matrices was detected in the FR-Film and UR-Film spectra, consistent with the presence of residual furcellaran and ulvan, respectively (Bojorges et al., 2022). Its lower intensity relative to the corresponding residues suggests a reduced contribution or a rearrangement of sulfated domains during processing. The decrease in the C–O–S vibration at ~850 cm^{-1} supported this interpretation, particularly in the *U. lactuca* based samples (Chi et al., 2020).

The glycosidic region showed changes common to most films. The band near ~1030 cm^{-1}, attributed to C–O–C stretching vibrations within polysaccharide backbones, became more defined after film formation (Freitas et al., 2022). A band around ~930 cm^{-1}, associated with β-glycosidic linkages, also became sharper in several films (Valério Filho et al., 2023). These spectral changes suggest that thermomechanical processing modified the local organization of polysaccharide chains, without eliminating the main glycosidic features of the residual matrices.

Among the residue-film pairs, the untreated *S. latissima* showed the clearest spectral modification after film formation. Compared with SR, the SR-Film spectrum displayed a sharper O–H stretching region between 3600 and 3000 cm^{-1}, suggesting changes in the hydrogen-bonding environment during processing and drying. The Amide I and II bands were attenuated, consistent with a lower spectroscopic contribution of proteinaceous components after thermomechanical processing. The sulfate-associated band around ~1240 cm^{-1} also decreased in intensity, indicating a reduced contribution of sulfated groups, possibly due to rearrangement or partial loss of these domains during processing. In contrast, bands associated with glycosidic linkages, particularly those near ~1030 and ~930 cm^{-1}, became more prominent and better resolved. These changes suggest that extrusion and hot pressing promoted a redistribution of the remaining polysaccharide and proteinaceous components in the SR matrix. The changes observed in *F. lumbricalis* and *U. lactuca* films were more moderate, consistent with the broader compositional heterogeneity and greater retention of residue-specific matrix components in these film-forming systems. After processing, the films retained the main polysaccharide-related bands observed in the residues, while the changes in band intensity and definition reflected residue-dependent differences in the processed matrices.

The nanostructural organization of the residues and their corresponding films was further examined by SAXS (Fig. 7). FR and SR showed a weak peak at approximately 0.14 $Å^{-1}$, corresponding to a real-space distance of ca. 4.5 nm, which has been associated with the center-to-center spacing between cellulose microfibrils in seaweed-derived cellulose-containing matrices (Cebrián-Lloret et al., 2023; Vega-Gómez et al., 2026). In FR, an additional contribution around 0.10 $Å^{-1}$ was observed, suggesting the presence of ordered domains involving non-cellulosic polysaccharides. UR showed a broader shoulder rather than a well-defined cellulose-related peak, consistent with less-resolved nanoscale organization and the contribution of ulvan-rich and other non-cellulosic fractions. A similar overlap of cellulose and non-cellulosic polysaccharide-associated features has been reported for native *Ulva* cell walls (Vega-Gómez et al., 2026).

The pigment-removal treatment modified these scattering features in a residue-dependent manner. In DS, the cellulose-related peak became sharper, although less intense, which is consistent with the partial removal of surrounding alginate- and fucoidan-associated fractions. This more defined SAXS feature contrasted with the inability of DS to form a continuous film, suggesting that processability depended on additional matrix-level factors beyond nanoscale ordering. By contrast, the defined

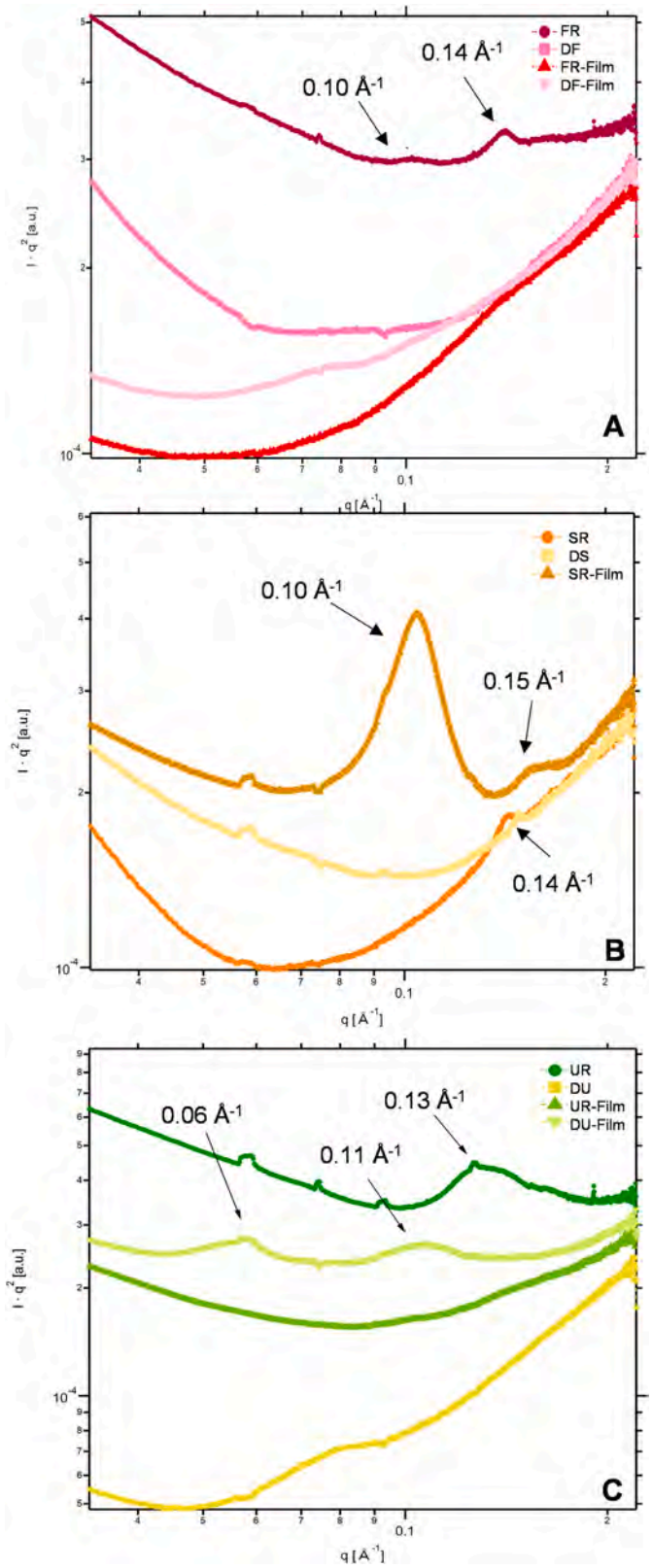

Fig. 7. SAXS Kratky plots of untreated and pigment-removed residues and their corresponding films.

features observed in FR and UR became less evident after treatment, indicating a reduction in the nanoscale contrast or ordering of mixed polysaccharide domains involving cellulose-associated and residual furcellaran or ulvan related fractions. In DU, the presence of a broad shoulder centered around 0.073 $Å^{-1}$, corresponding to a real-space distance of ca. 8.6 nm, suggested that some residual nanoscale organization remained after treatment. These differences indicate that the nanoscale response to pigment removal depended on the initial residual matrix architecture, including both macroalgal origin and prior extraction history.

Film formation introduced additional changes in the SAXS profiles. In FR-Film and UR-Film, the ordered features detected in the corresponding residues became less defined, suggesting partial disruption or redistribution of polysaccharide domains during extrusion and hot pressing. In contrast, SR-Film showed a more intense peak centered around 0.10 $Å^{-1}$, accompanied by a weaker contribution near 0.15 $Å^{-1}$. This pattern suggests that thermomechanical processing promoted a change in the spatial organization of cellulose-associated and residual alginate-rich domains in the SR matrix. A restructuring effect was also observed in films obtained from pigment-removed residues, particularly in DU-Film, where broad shoulders appeared around 0.06 and 0.11 $Å^{-1}$. Such behavior is consistent with the capacity of semicrystalline polysaccharide domains to reorganize during heating-cooling processes. This interpretation is consistent with the compositional shifts and FTIR changes described above, which indicate residue-dependent modification of proteinaceous and non-cellulosic polysaccharide fractions after pigment removal.

WAXS analysis provided complementary information on the crystalline organization of the residues and films (Fig. 8). The crystallinity index values calculated from the WAXS profiles are reported as apparent crystallinity indices (Table 3), considering the heterogeneous composition of the residual matrices and the possible contribution of non-cellulosic ordered phases.

FR showed the highest apparent crystallinity among the untreated residues (25.8%). However, this value may include contributions from inorganic crystalline salts present in the biomass or introduced during industrial processing, in agreement with the relatively high ash content of this residue (Table 1) (Cian et al., 2015). After pigment-removal treatment, the crystallinity of DF decreased to 7.3%, consistent with the attenuation of ordered SAXS features. This decrease suggests a lower contribution of crystalline or semi-ordered domains after treatment, rather than a selective loss of cellulose organization alone. Film formation reduced the apparent crystallinity of FR-Film to 11.9%, whereas DF-Film showed a partial increase relative to DF, reaching 16.7%. This increase may reflect processing-induced rearrangement of residual polysaccharide-rich domains, together with possible salt redistribution or recrystallization. Therefore, the apparent crystallinity increase in DF-Film should not be attributed exclusively to cellulose reorganization.

A different trend was observed for *S. latissima*. The pigment-removal treatment increased the crystallinity index from 12.1% in SR to 23.6% in DS, consistent with the sharper cellulose-related SAXS feature and with the cellulose enrichment and marked reduction of uronic acid rich fractions detected compositionally. Similar increases in cellulose crystallinity after selective removal of amorphous components have been reported for algal and lignocellulosic residues (Cheng et al., 2015; Liu et al., 2019). However, DS did not form a film under the processing conditions used, indicating that the increase in crystalline contribution was not sufficient to maintain matrix continuity. In SR-Film, the crystallinity index increased slightly to 14.4%, suggesting that extrusion and hot pressing induced only moderate reorganization of the untreated SR matrix.

For *U. lactuca*, UR showed an apparent crystallinity of 20.9%, which decreased markedly to 5.0% after pigment-removal treatment. This drop was consistent with the SAXS profile, where the broad ordered features became less defined after treatment, and suggests a reduction in the ordered contribution of ulvan-associated and cellulose-containing domains. After film formation, UR-Film retained a crystallinity close to that of the untreated residue (19.4%), whereas DU-Film showed a marked increase relative to DU, reaching 24.6%. This increase in DU-Film may be associated with thermal rearrangement and packing of

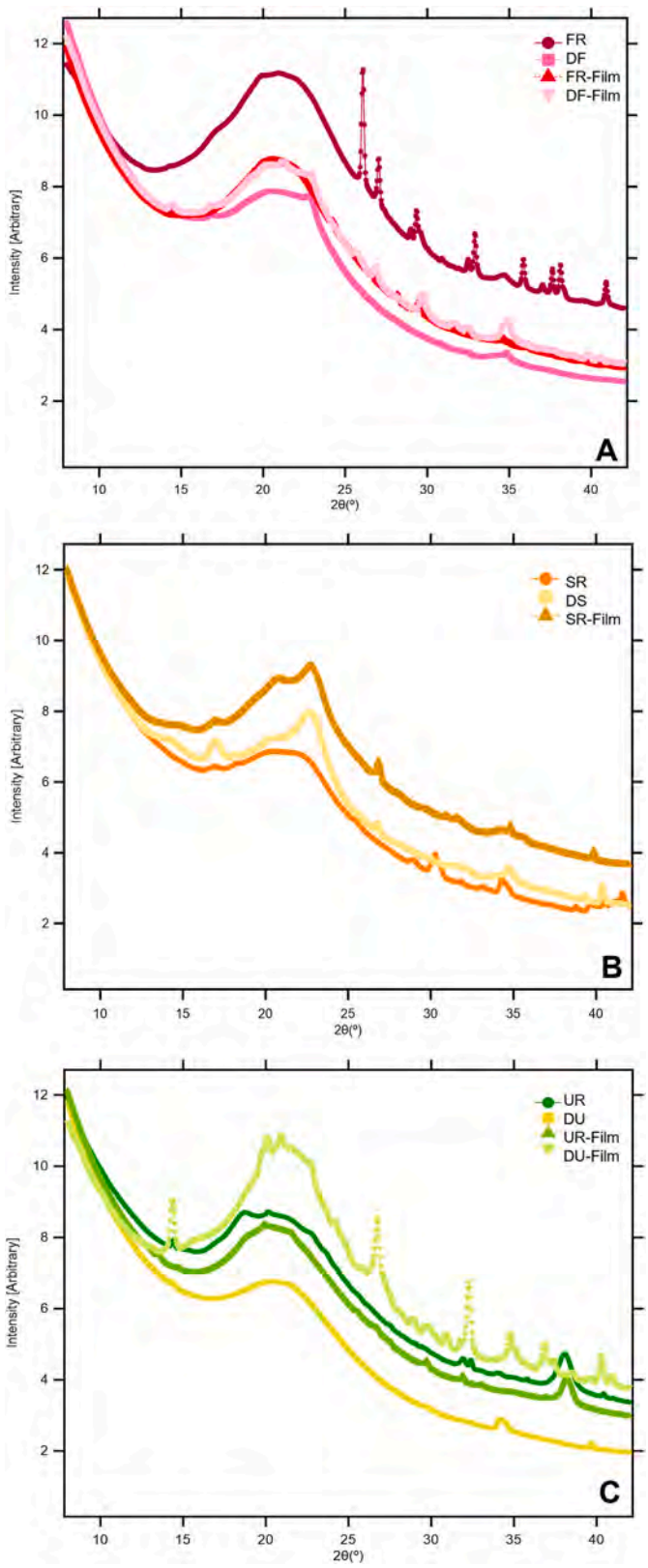

Fig. 8. WAXS patterns of untreated and pigment-removed residues and their corresponding films.

residual polysaccharide-rich domains during extrusion and hot pressing. However, contributions from inorganic salts cannot be ruled out, given the high ash content of *U. lactuca* residues (Table 1).

The position and relative intensity of WAXS reflections further supported the residue-dependent organization of cellulose and associated polysaccharides. In SR and DS, diffraction features near 22° were consistent with the (200) reflection of cellulose I, accompanied by weaker contributions around 15° and 16.4° assigned to the (1–10) and (110) planes, respectively (French, 2014; Martínez-Sanz et al., 2020). These positions fall within the range reported for plant and marine cellulose microfibrils (Nurhayati et al., 2025). The sharper contribution observed in DS was consistent with the lower contribution of the surrounding non-cellulosic matrix fractions after the pigment-removal treatment, as reflected in the increase in apparent crystallinity.

Table 3
Crystallinity index (Xc) values of untreated and pigment-removed seaweed residues and their corresponding films.

Treatment	Sample	Xc (%)
Residue		
Untreated	FR	25.8
	SR	12.1
	UR	20.9
Pigment-removed	DF	7.3
	DS	23.6
	DU	5.0
Film		
Untreated	FR-Film	11.9
	SR-Film	14.4
	UR-Film	19.4
Pigment-removed	DF-Film	16.7
	DU-Film	24.6

In SR-Film, the same reflection was retained but became broader and less intense, suggesting that extrusion and compression molding altered the packing or local order of cellulose-rich domains. Similar processing-induced changes in cellulose diffraction profiles have been reported for mechanically or thermomechanically treated lignocellulosic materials (Kantrong et al., 2024; Park et al., 2010). FR and UR showed less resolved cellulose-I reflections, consistent with more heterogeneous matrices in which cellulose was embedded within furcellaran or ulvan containing residual matrices. After film formation, DF-Film showed a broad, low-intensity contribution near 22°. In contrast, DU-Film did not display a clearly resolved cellulose-I reflection, indicating that the ordered domains in these films cannot be attributed solely to cellulose crystallinity. This behavior is consistent with the SAXS results, which showed broad nanoscale features rather than well-defined cellulose-associated ordering in DU-Film.

3.5.3. *Thermal properties of the films*

The thermal behavior of the films was evaluated using differential scanning calorimetry (DSC). As shown in Fig. 9, all thermograms exhibited an initial endothermic event between 40 and 120 °C, mainly associated with water evaporation/desorption from the hydrophilic regions of the residue-based matrices (Albertos et al., 2019). The temperature and intensity of this transition varied across the films, reflecting differences in matrix-water interactions.

SR-Film, UR-Film, and DU-Film exhibited endothermic events mainly between 40 and 100 °C, consistent with the release of less strongly retained water. In SR-Film, this transition appeared sharper and more intense, suggesting a more defined water-associated thermal event within the matrix. In UR-Film and DU-Film, the broader transitions were consistent with a more heterogeneous distribution of water-binding sites, likely related to the presence of ulvan-related polysaccharides, minerals, and other hydrophilic residual components.

By contrast, FR-Film and DF-Film showed broader endothermic signals shifted toward higher temperatures, mainly between 90 and 120 °C. This behavior suggests a larger contribution of more strongly retained water, which may be associated with the comparatively compact morphology observed by SEM and with the protein-polysaccharide-rich composition of *F. lumbricalis* residues. The higher protein content of these films could contribute to a more cohesive matrix in which water

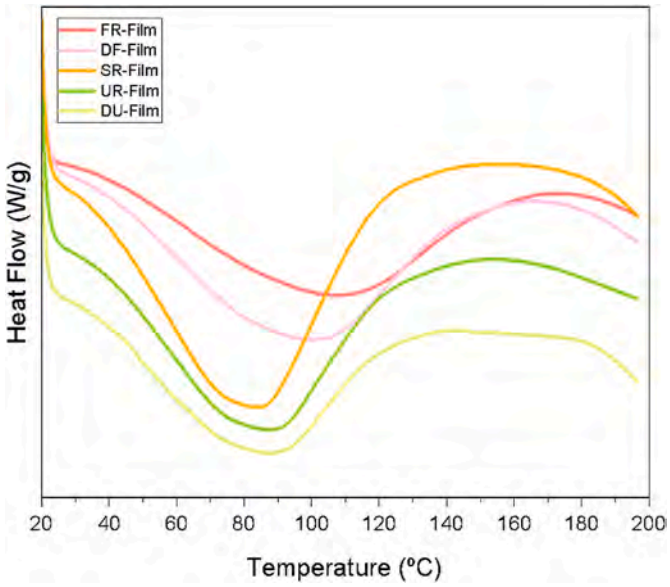

Fig. 9. DSC thermograms of films developed from untreated and pigment-removed residues.

desorption occurs over a higher temperature range.

The pigment-removal treatment produced moderate but formulation-dependent changes in the low-temperature endothermic region. In DF-Film and DU-Film, the transition shifted slightly toward higher temperatures and decreased in intensity. This response may reflect changes in the availability and distribution of hydrophilic domains after partial removal of soluble polysaccharides, proteins, and lipids from the starting residues. The effect was not uniform across residue-based matrices, consistent with the compositional, FTIR, and morphological differences observed after the pigment-removal treatment. Within the temperature range analyzed, the DSC profiles were therefore mainly governed by water-associated transitions rather than by clearly resolved polymer degradation events. These thermal responses were consistent with the residue-dependent matrix organization observed by SEM and provide additional evidence of differences in water-matrix interactions among the films.

3.5.4. *Mechanical and barrier properties*

The mechanical properties of the films were assessed by tensile testing, and the results from the stress-strain curves are presented in Table 4. Because the conditioned films reached formulation-dependent equilibrium moisture contents, tensile performance was interpreted considering both moisture-induced plasticization and residual matrix cohesion, the latter reflecting macroalgal origin, prior extraction history, and pigment-removal-induced compositional changes.

Among films prepared from untreated residues, FR-Film showed the highest elastic modulus and tensile strength, reaching 373.7 MPa and 8.0 MPa, respectively. This behavior is consistent with the compact cross-sectional morphology observed by SEM and with the high protein content of *F. lumbricalis* residues (Table 1). Proteinaceous fractions can promote intermolecular interactions with polysaccharides through hydrogen bonding, electrostatic associations, and, in some cases, covalent cross-linking, contributing to the cohesion of biopolymer networks (Calva-Estrada et al., 2019; Karakuş, 2025). In FR-Film, these interactions may have favored the integration of cellulose-rich and galactan-associated domains into a comparatively rigid matrix. The relatively low moisture content of FR-Film (22.8 ± 0.6%) may also have contributed to its higher stiffness by limiting water-induced plasticization.

SR-Film exhibited the lowest modulus and tensile strength, but the highest elongation at break. This profile suggests a softer and more deformable matrix, consistent with the presence of residual alginate-associated fractions in *S. latissima*. Alginate-rich domains are highly hydrated and can increase chain mobility within composite hydrogel-like networks, leading to lower stiffness and higher extensibility (Aarstad et al., 2017; Bojorges et al., 2022). This interpretation is supported by the highest measured moisture content in SR-Film (33.0 ± 0.3%), indicating a stronger water-plasticized response under the conditioning conditions used. The fact that SR-Film remained extensible despite its cellulose content reinforces the idea that mechanical behavior was not governed by cellulose enrichment alone, but by the contribution of the surrounding amorphous matrix.

UR-Film showed intermediate mechanical properties, with moderate stiffness and elongation. This response is consistent with the ulvan-rich composition of *U. lactuca* residues, where sulfated and uronic acid containing polysaccharides may contribute to both cohesion and flexibility through hydrogen bonding and ionic interactions. Its intermediate moisture content (25.9 ± 0.0%) was consistent with a matrix less water-plasticized than SR-Film but more hydrophilic than FR-Film. The more heterogeneous morphology observed by SEM likely limited the development of the higher strength observed in FR-Film.

The pigment-removal treatment reduced the mechanical performance of the films that could be formed from treated residues. In DF-Film, both modulus and tensile strength decreased relative to FR-Film, despite the higher apparent crystallinity observed after film formation (Table 3). This decrease is consistent with the partial removal of proteins and non-cellulosic matrix components during pigment removal (Table 1), which likely reduced the number of cohesive interactions available during processing. The similar moisture contents of FR-Film and DF-Film (22.8 ± 0.6% and 21.7 ± 1.2%, respectively) indicate that the decrease in mechanical performance after treatment was not primarily due to increased moisture-induced plasticization, but rather to changes in matrix composition and cohesion.

A similar trend was observed for DU-Film, which showed lower stiffness and strength than UR-Film. In this case, the reduction in mechanical performance may be related to the partial loss of ulvan-associated domains and minor hydrophobic fractions, together with

Table 4
Moisture content, thickness, tensile properties, water vapor permeability, and water uptake of films prepared from untreated and pigment-removed seaweed residues.

Properties	FR-Film	SR-Film	UR-Film	DF-Film	DU-Film
Moisture (%)	22.8 ± 0.6^{a}	33.0 ± 0.3^{d}	25.9 ± 0.0^{b}	21.7 ± 1.2^{a}	28.1 ± 0.9^{c}
Thickness (mm)	0.14 ± 0.0^{a}	0.14 ± 0.0^{a}	0.15 ± 0.0^{a}	0.14 ± 0.0^{a}	0.20 ± 0.0^{b}
Tensile properties					
E (MPa)	373.7 ± 24.1^{d}	32.4 ± 9.9^{a}	131.1 ± 24.7^{c}	150.5 ± 19.7^{c}	69.2 ± 10.7^{b}
TS (MPa)	8.0 ± 0.5^{d}	2.7 ± 0.1^{a}	4.2 ± 0.3^{c}	3.6 ± 0.2^{b}	2.5 ± 0.2^{a}
ϵ_b(%)	6.6 ± 0.2^{a}	11.7 ± 3.6^{b}	9.6 ± 2.5^{ab}	6.6 ± 0.8^{a}	6.4 ± 0.1^{a}
Water vapor permeability					
WVP 10^{-13} (Kg·m·Pa^{-1} s^{-1} m^{-2})	2.4 ± 0.1^{a}	7.2 ± 0.1^{c}	8.5 ± 0.5^{d}	4.9 ± 0.2^{b}	9.6 ± 0.1^{e}
Water uptake (%)	12.1 ± 1.2^{ab}	16.6 ± 1.1^{bc}	19.8 ± 0.9^{c}	11.0 ± 1.3^{a}	25.1 ± 1.2^{d}

Values are expressed as means ± SD ($n \geq 3$, except tensile properties where $n \geq 6$). Different letters within the same row indicate significant differences ($p < 0.05$). E, elastic modulus; TS, tensile strength; εb, elongation at break; WVP, water vapor permeability.

the more discontinuous morphology observed in the cross-section. Although DU-Film showed the highest thickness and a higher moisture content than UR-Film (28.1 ± 0.9% and 25.9 ± 0.0%, respectively), its lower elongation suggests that water uptake alone did not determine deformability; instead, the loss of cohesive matrix components and the formation of a less continuous structure likely constrained mechanical performance.

These results show that higher apparent crystallinity did not necessarily translate into improved mechanical performance. Instead, the tensile response of the films was strongly influenced by equilibrium moisture content together with the ability of each residual matrix to maintain cohesive protein-polysaccharide and non-cellulosic domains during thermomechanical processing. The measured tensile values are within the range reported for several cellulose-based and residue-derived biopolymer films, indicating that selected seaweed residue-based films can provide packaging-relevant mechanical integrity without requiring purified film-forming polymers (Freitas et al., 2022; Sirviö et al., 2023).

Water vapor permeability (WVP) was strongly influenced by the film composition and microstructure (Table 4). Since film thickness was incorporated into the WVP calculation, the permeability differences are more appropriately interpreted in relation to matrix continuity, hydrophilicity, and microstructural organization. FR-Film showed the lowest WVP value 2.4 ± 0.1 × 10^{-13} kg m·m^{-2}·s^{-1}·Pa^{-1}, consistent with its compact cross-section and higher protein content. The presence of proteinaceous and galactan-rich fractions may have contributed to matrix cohesion, reducing the number of preferential pathways for water vapor diffusion. In contrast, SR-Film and UR-Film exhibited higher WVP values, 7.2 ± 0.1 and 8.5 ± 0.5 × 10^{-13} kg m·m^{-2}·s^{-1}·Pa^{-1}, respectively, consistent with their more hydrophilic, polysaccharide-rich composition and less compact morphology.

The pigment-removal treatment did not improve the water-vapor barrier of the treated films. Both DF-Film and DU-Film showed higher WVP values than their untreated counterparts, despite the increase in apparent crystallinity observed after film formation (Table 3). This behavior indicates that crystalline contribution alone did not govern water vapor transport. In DF-Film, the increase in WVP from 2.4 ± 0.1 to 4.9 ± 0.2 × 10^{-13} kg m·m^{-2}·s^{-1}·Pa^{-1}may be related to the partial removal of proteinaceous and non-cellulosic components that contributed to matrix cohesion in FR-Film. In DU-Film, the higher permeability (9.6 ± 0.1 × 10^{-13} kg m·m^{-2}·s^{-1}·Pa^{-1}) was consistent with the loss of minor hydrophobic fractions, the high mineral content of the residue, and the more discontinuous morphology observed by SEM. These factors likely increased the number of preferential pathways for water diffusion, offsetting any barrier improvement expected from higher crystalline order. Similar behavior has been reported for cellulose-based films, where increased purification or removal of amorphous components did not necessarily improve barrier performance when cohesive matrix domains were also lost (Martínez-Sanz et al., 2020).

The WVP values obtained here were higher than those reported for holocellulosic-fraction films prepared from marine biomass and for cellulose-based films containing residual agar (Benito-González et al., 2018; Martínez-Sanz et al., 2020). This comparison suggests that water-vapor barrier performance remains a limitation of these unpurified residue-based films, particularly for applications under high-humidity conditions. However, differences among species provide useful insights into how residual matrix composition governs moisture transport in seaweed-residue-based films.

Water uptake followed a similar matrix-dependent trend (Table 4). UR-Film showed the highest water uptake among the untreated films, 19.8 ± 0.9%, consistent with the hydrophilic nature of ulvan-type polysaccharides and the high mineral content of *U. lactuca* residues. Uronic acid- and sulfate-containing polysaccharides provide multiple sites for hydrogen bonding and electrostatic interactions with water molecules, which can favor moisture sorption in hydrated matrices (Agles & Bourg, 2024; Etale et al., 2023). SR-Film also showed relatively high-water uptake (16.6 ± 1.1%), in agreement with the contribution of alginate-associated domains. By contrast, FR-Film exhibited the lowest water uptake (12.1 ± 1.2%), consistent with its more compact morphology and higher proportion of proteinaceous and lipid fractions.

The effect of pigment removal on water uptake was also residue-dependent. DU-Film showed the highest water uptake among all films (25.1 ± 1.2%), consistent with the partial lipid removal and disruption of ulvan-associated domains, which may have increased the exposure of hydrophilic groups and facilitated water retention. In contrast, DF-Film maintained a comparatively low water uptake (11.0 ± 1.3%), suggesting that the remaining protein- and galactan-rich matrix still restricted water accessibility after treatment. This behavior aligns with previous reports showing that polysaccharide-rich films, particularly those based on cellulose derivatives or starch, generally exhibit greater moisture affinity than protein-rich matrices due to the abundance of accessible hydroxyl groups (Gökkaya Erdem et al., 2021; Wilpiszewska et al., 2020).

3.5.5. *Surface wettability of the films*

Water contact angle measurements were used to evaluate the surface wettability of the films (Fig. 10). The values ranged from approximately 47° to 67°, consistent with the water-affine character expected for polysaccharide-rich residue-based matrices. However, clear differences were observed among species and treatments, indicating that surface wettability was influenced not only by the overall composition of the films but also by the components exposed at the film-water interface.

FR-Film and SR-Film showed the highest contact angles, indicating comparatively lower wettability. In FR-Film, this behavior may be associated with its higher protein content and compact morphology, which could reduce the accessibility of surface-bound highly hydrophilic polysaccharide domains. In SR-Film, the relatively high contact angle suggests that alginate-associated hydrophilic fractions were not predominantly exposed at the outer film surface, despite their contribution to the bulk water affinity of the matrix. This distinction is relevant because the contact angle reflects the initial surface response to water, whereas water uptake and WVP depend on both the surface and the bulk matrix organization.

Films derived from *U. lactuca* showed lower contact angles, particularly DU-Film, indicating greater surface wettability. This behavior aligns with the hydrophilic nature of ulvan-related polysaccharides, which contain sulfate and uronic acid groups that interact strongly with water. The high mineral content of *U. lactuca* residues may also contribute to water affinity at the surface. Although UR contained a

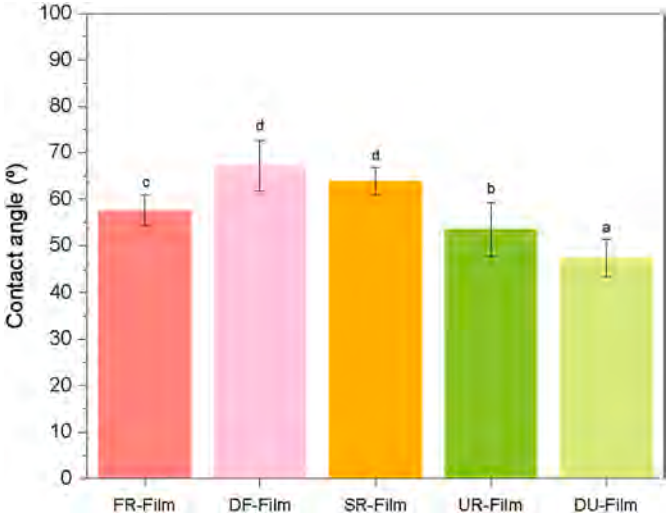

Fig. 10. Water contact angle values of films obtained from untreated and pigment-removed residues.

small lipid fraction, it was insufficient to produce a more hydrophobic surface, probably because hydrophilic polysaccharide and mineral associated domains remained dominant at the interface. Similar behavior has been reported in biopolymer films where surface wettability depends on the distribution and accessibility of hydrophilic components rather than on the mere presence of minor hydrophobic fractions (Galus & Kadzińska, 2016).

The pigment-removal treatment affected surface wettability differently across species. In *F. lumbricalis*, the contact angle increased after treatment, suggesting reduced exposure of highly hydrophilic domains at the surface of the DF-Film. This change may be associated with the partial removal of soluble carbohydrate fractions, together with the persistence of a comparatively cohesive protein-polysaccharide matrix. In *U. lactuca*, pigment removal decreased the contact angle, indicating a more water-affine surface in DU-Film. This response is consistent with the loss of minor hydrophobic fractions and the increased relative contribution of hydrophilic ulvan-associated and mineral-rich domains after treatment. The opposite responses of DF-Film and DU-Film are consistent with matrix-dependent changes in the surface composition induced by the pigment-removal treatment.

4. Conclusions

Seaweed biorefinery residues obtained after furcellaran extraction from *Furcellaria lumbricalis*, alginate extraction from *Saccharina latissima*, and protein extraction from *Ulva lactuca* were evaluated as complex residue-based film-forming matrices rather than purified polysaccharide or cellulose-rich fractions. All untreated residues formed self-supporting films, but their performance was strongly residue-specific, reflecting differences in macroalgal origin, prior extraction history, and residual matrix composition. H_2O_2/UV-assisted pigment removal improved residue whiteness but produced matrix-dependent effects on film formation and functionality. The *F. lumbricalis* residue retained sufficient protein-polysaccharide connectivity after the pigment-removal treatment to produce cohesive films with comparatively high mechanical strength, low water uptake, low WVP, and improved optical appearance, identifying this residue as the most promising matrix among those evaluated for further formulation. In contrast, pigment-removed *S. latissima* did not form a continuous film, despite its numerically higher cellulose content and increased apparent crystallinity, highlighting that cellulose enrichment or crystalline contribution alone was insufficient to ensure processability under the processing conditions used. Films from *U. lactuca* remained processable but showed higher water affinity and permeability, consistent with their ulvan-rich, mineral-containing, and less compact matrix. These results indicate that the functional value of pigment removal depends on preserving residual polymer connectivity rather than on whitening or purification alone. These findings establish a structure-function basis for selecting seaweed biorefinery residues as packaging-oriented film-forming matrices, providing the groundwork for subsequent formulation optimization and application-specific validation in food-packaging systems.

CRediT authorship contribution statement

Hylenne Bojorges: Conceptualization, Data curation, Formal analysis, Methodology, Visualization, Writing – original draft, Writing – review & editing. **Yubexi Correa:** Data curation, Formal analysis, Investigation, Writing – original draft, Writing – review & editing. **Marta Martínez-Sanz:** Investigation, Methodology, Writing – review & editing. **Amparo López-Rubio:** Conceptualization, Funding acquisition, Methodology, Project administration, Writing – review & editing. **María José Fabra:** Conceptualization, Investigation, Methodology, Project administration, Supervision, Writing – review & editing.

Declaration of competing interests

The authors declare that there are no conflicts of interest.

Acknowledgements

The authors acknowledge financial support from grants PID2022-138328OB-C21 and CEX2021-001189-S, funded by MCIN/AEI/10.13039/501100011033 and the European Regional Development Fund (ERDF, "A way of making Europe"), as well as grant PCI2024-153420, funded by MICIU/AEI/10.13039/501100011033 and the European Union. This work was carried out within the framework of the SEAFOODTURE project (Proposal SBEP2023-39), funded by the Sustainable Blue Economy Partnership (SBEP) Joint Call 2023; ERANET Call 2023). The authors also acknowledge financial support from the EVOLVEPACK project, which contributes to the PRIMA Programme (Partnership for Research and Innovation in the Mediterranean Area), funded through the European Union's Horizon 2020 Framework Programme and national research funding agencies (PCI2024-153409).

Appendix A. Supplementary data

Supplementary data to this article can be found online at https://doi.org/10.1016/j.foodhyd.2026.113247.

Data availability

Data will be made available on request.

References

Aaliya, B., Sunooj, K. V., & Lackner, M. (2021). Biopolymer composites: A review. *International Journal of Biobased Plastics, 3*(1), 40–84. https://doi.org/10.1080/24759651.2021.1881214

Aarstad, O., Heggset, E. B., Pedersen, I. S., Bjørnøy, S. H., Syverud, K., & Strand, B. L. (2017). Mechanical properties of composite hydrogels of alginate and cellulose nanofibrils. *Polymers, 9*(8), 378. https://doi.org/10.3390/POLYM9080378, 2017, Vol. 9, Page 378.

Agles, A. A., & Bourg, I. C. (2024). Structure and dynamics of water in polysaccharide (Alginate) solutions and gels explained by the core-shell model. *Biomacromolecules, 25*(10), 6403–6415. https://doi.org/10.1021/ACS.BIOMAC.4C00447/ASSET/IMAGES/LARGE/BM4C00447_0007.JPEG

Albertos, I., Martin-Diana, A. B., Burón, M., & Rico, D. (2019). Development of functional bio-based seaweed (Himanthalia elongata and Palmaria palmata) edible films for extending the shelflife of fresh fish burgers. *Food Packaging and Shelf Life, 22*, Article 100382. https://doi.org/10.1016/J.FPSL.2019.100382

Alboofetileh, M., Jeddi, S., Subi, T. M., & Vasanthi, H. R. (2025). Sulfated polysaccharides from Ulva rigida as antioxidant and antibacterial enhancers in chicken sausages. *Algal Research, 86*, Article 103940. https://doi.org/10.1016/J.ALGAL.2025.103940

Amarowicz, R. (2009). Antioxidant activity of maillard reaction products. *European Journal of Lipid Science and Technology, 111*(2), 109–111. https://doi.org/10.1002/EJLT.200900011

Angell, A. R., Mata, L., de Nys, R., & Paul, N. A. (2016). The protein content of seaweeds: A universal nitrogen-to-protein conversion factor of five. *Journal of Applied Phycology, 28*(1), 511–524. https://doi.org/10.1007/S10811-015-0650-1/FIGURES/5

AOAC. (1990). *Official methods of analysis of the Association of official Analytical Chemists* (9th ed.). Association of Official Analytical Chemists [Book].

Athanasopoulou, E., Bigi, F., Maurizzi, E., Karellou, E. I. E., Pappas, C. S., Quartieri, A., & Tsironi, T. (2024). Synthesis and characterization of polysaccharide- and protein-based edible films and application as packaging materials for fresh fish fillets. *Scientific Reports 2024, 14*(1), 517. https://doi.org/10.1038/s41598-024-51163-y, 14(1.

Bealer, E. J., Onissema-Karimu, S., Rivera-Galletti, A., Francis, M., Wilkowski, J., de la Cruz, D. S., & Hu, X. (2020). Protein–Polysaccharide composite materials: Fabrication and applications. *Polymers, 12*(2), 464. https://doi.org/10.3390/POLYM12020464, 2020, Vol. 12, Page 464.

Benito-González, I., López-Rubio, A., & Martínez-Sanz, M. (2018). Potential of lignocellulosic fractions from Posidonia oceanica to improve barrier and mechanical properties of bio-based packaging materials. *International Journal of Biological Macromolecules, 118*, 542–551. https://doi.org/10.1016/J.IJBIOMAC.2018.06.052

Bertaud, F., Sundberg, A., & Holmbom, B. (2002). Evaluation of acid methanolysis for analysis of wood hemicelluloses and pectins. *Carbohydrate Polymers, 48*(3), 319–324. https://doi.org/10.1016/S0144-8617(01)00249-1

Besednova, N. N., Andryukov, B. G., Zaporozhets, T. S., Kryzhanovsky, S. P., Kuznetsova, T. A., Fedyanina, L. N., Makarenkova, I. D., & Zvyagintseva, T. N.

(2020). Algae polyphenolic compounds and modern antibacterial strategies: Current achievements and immediate prospects. *Biomedicines, 8*(9), 342. https://doi.org/10.3390/BIOMEDICINES8090342

Blanco-Pascual, N., Montero, M. P., & Gómez-Guillén, M. C. (2014). Antioxidant film development from unrefined extracts of brown seaweeds Laminaria digitata and Ascophyllum nodosum. *Food Hydrocolloids, 37*, 100–110. https://doi.org/10.1016/J.FOODHYD.2013.10.021

Bojorges, H., Fabra, M. J., López-Rubio, A., & Martínez-Abad, A. (2022). Alginate industrial waste streams as a promising source of value-added compounds valorization. *Science of The Total Environment, 838*, Article 156394. https://doi.org/10.1016/J.SCITOTENV.2022.156394

Bojorges, H., López-Rubio, A., Fabra, M. J., & Martínez-Abad, A. (2023). Estimation of alginate purity and M/G ratio by methanolysis coupled with anion exchange chromatography. *Carbohydrate Polymers, 321*, Article 121285. https://doi.org/10.1016/j.carbpol.2023.121285

Bojorges, H., López-Rubio, A., Martínez-Abad, A., & Fabra, M. J. (2025). Functional and bioactive properties of the protein-polysaccharide extracts from brown algae: Exploring novel functional ingredients. *Food Hydrocolloids, 162*, Article 110967. https://doi.org/10.1016/J.FOODHYD.2024.110967

Bojorges, H., Martínez-Sanz, M., Fontes-Candia, C., Díaz-Piñero, L., Martínez-Abad, A., López-Rubio, A., & Fabra, M. J. (2025). Protein extraction from the industrial solid residue of brown seaweed after alginate extraction. *Food Hydrocolloids, 159*, Article 110708. https://doi.org/10.1016/j.foodhyd.2024.110708

Bruhns, P., Kanzler, C., Degenhardt, A. G., Koch, T. J., & Kroh, L. W. (2019). Basic structure of melanoidins formed in the maillard reaction of 3-Deoxyglucosone and γ-Aminobutyric acid. *Journal of Agricultural and Food Chemistry, 67*(18), 5197–5203. https://doi.org/10.1021/ACS.JAFC.9B00202/ASSET/IMAGES/LARGE/JF-2019-002025_0008.JPEG

Calva-Estrada, S. J., Jiménez-Fernández, M., & Lugo-Cervantes, E. (2019). Protein-Based films: Advances in the development of biomaterials applicable to food packaging. *Food Engineering Reviews, 11*(2), 78–92. https://doi.org/10.1007/S12393-019-09189-W, 2019 11:2.

Cebrián-Lloret, V., Martínez-Abad, A., López-Rubio, A., & Martínez-Sanz, M. (2023). Sustainable bio-based materials from minimally processed red seaweeds: Effect of composition and cell Wall structure. *Journal of Polymers and the Environment, 31*(3), 886–899. https://doi.org/10.1007/S10924-022-02648-2/FIGURES/6

Chang, S., Chen, X., Chen, Y., You, L., & Hileuskaya, K. (2023). UV/H2O2-Degraded polysaccharides from sargassum fusiforme: Purification, structural properties, and anti-inflammatory activity. *Marine Drugs, 21*(11). https://doi.org/10.3390/MD21110561

Cheng, G., Zhang, X., Simmons, B., & Singh, S. (2015). Theory, practice and prospects of X-ray and neutron scattering for lignocellulosic biomass characterization: Towards understanding biomass pretreatment. *Energy & Environmental Science, 8*(2), 436–455. https://doi.org/10.1039/C4EE03147D

Chi, Y., Li, H., Wang, P., Du, C., Ye, H., Zuo, S., Guan, H., & Wang, P. (2020). Structural characterization of ulvan extracted from Ulva clathrata assisted by an ulvan lyase. *Carbohydrate Polymers, 229*, Article 115497. https://doi.org/10.1016/J.CARBPOL.2019.115497

Cian, R. E., Drago, S. R., De Medina, F. S., & Martínez-Augustin, O. (2015). Proteins and carbohydrates from red seaweeds: Evidence for beneficial effects on gut function and microbiota. *Marine Drugs, 13*(8), 5358–5383. https://doi.org/10.3390/MD13085358. *2015, Vol. 13, Pages 5358-5383*.

Davies, M. J. (2016). Protein oxidation and peroxidation. *Biochemical Journal, 473*(Pt 7), 805. https://doi.org/10.1042/BJ20151227

Díaz-Montes, E. (2022). Polysaccharide-Based biodegradable films: An alternative in food packaging. *Polysaccharides, 3*(4), 761–775. https://doi.org/10.3390/POLYSACCHARIDES3040044, 2022, Vol. 3, Pages 761-775.

Dutra, E. D., Santos, F. A., Alencar, B. R. A., Reis, A. L. S., de Souza, R. de F. R., Aquino, K. A. da S., Morais Jr, M. A., & Menezes, R. S. C. (2018). Alkaline hydrogen peroxide pretreatment of lignocellulosic biomass: Status and perspectives. *Biomass Conversion and Biorefinery, 8*(1), 225–234. https://doi.org/10.1007/s13399-017-0277-3

Eha, K., Onis Pehk, T., Heinmaa, I., Kaleda, A., & Laos, K. (2017). Impact of short-term heat treatment on the structure and functional properties of commercial furcellaran compared to commercial carrageenans. *Heliyon, e06640*, Article e06640. https://doi.org/10.1016/j.heliyon.2021.e06640

Etale, A., Onyianta, A. J., Turner, S. R., & Eichhorn, S. J. (2023). Cellulose: A review of water interactions, applications in composites, and water treatment. *Chemical Reviews, 123*(5), 2016–2048. https://doi.org/10.1021/ACS.CHEMREV.2C00477/ASSET/IMAGES/LARGE/CR2C00477_0024.JPEG

Fabra, M. J., Talens, P., & Chiralt, A. (2009). Microstructure and optical properties of sodium caseinate films containing oleic acid–beeswax mixtures. *Food Hydrocolloids, 23*(3), 676–683. https://doi.org/10.1016/J.FOODHYD.2008.04.015

Freitas, P. A. V., González-Martínez, C., & Chiralt, A. (2022). Applying ultrasound-assisted processing to obtain cellulose fibres from rice straw to be used as reinforcing agents. *Innovative Food Science & Emerging Technologies, 76*, Article 102932. https://doi.org/10.1016/J.IFSET.2022.102932

Freitas, P. A. V., Santana, L. G., González-Martínez, C., & Chiralt, A. (2024). Combining subcritical water extraction and bleaching with hydrogen peroxide to obtain cellulose fibres from rice straw. *Carbohydrate Polymer Technologies and Applications, 7*, Article 100491. https://doi.org/10.1016/J.CARPTA.2024.100491

French, A. D. (2014). Idealized powder diffraction patterns for cellulose polymorphs. *Cellulose, 21*(2), 885–896. https://doi.org/10.1007/S10570-013-0030-4/FIGURES/5

Fuertes-Rabanal, M., Rebaque, D., Largo-Gosens, A., Encina, A., & Mélida, H. (2025). Cell walls: A comparative view of the composition of cell surfaces of plants, algae, and microorganisms. *Journal of Experimental Botany, 76*(10), 2614–2645. https://doi.org/10.1093/jxb/erae512

Galus, S., & Kadzińska, J. (2016). Moisture sensitivity, optical, mechanical and structural properties of Whey protein-based edible films incorporated with rapeseed oil. *Food Technology and Biotechnology, 54*(1), 78. https://doi.org/10.17113/FTB.54.01.16.3889

Gökkaya Erdem, B., Dıblan, S., & Kaya, S. (2021). A comprehensive Study on sorption, water barrier, and physicochemical properties of some Protein- and carbohydrate-based edible films. *Food and Bioprocess Technology, 14*(11), 2161–2179. https://doi.org/10.1007/S11947-021-02712-0/FIGURES/4

Gómez, I., & Huovinen, P. (2020). Brown algal phlorotannins: An overview of their functional roles. In I. Gómez, & P. Huovinen (Eds.), *Antarctic seaweeds: Diversity, adaptation and ecosystem services* (pp. 365–388). Springer International Publishing. https://doi.org/10.1007/978-3-030-39448-6_18.

Gordalina, M., Pinheiro, H. M., Mateus, M., da Fonseca, M. M. R., & Cesário, M. T. (2021). Macroalgae as protein Sources—A review on protein bioactivity, extraction, purification and characterization. *Applied Sciences, 11*(17). https://doi.org/10.3390/app11177969

Hernández-García, E., Fabra, M. J., Reyes, A., & López-Rubio, A. (2026). Exploring the use of invasive algae Rugulopteryx okamurae and Gelidium corneum holocellulosic residue as additives in starch-based to develop sustainable materials. *Food Hydrocolloids, 179*, Article 112731. https://doi.org/10.1016/J.FOODHYD.2026.112731

Ilavsky, J., & Jemian, P. R. (2009). Irena: Tool suite for modeling and analysis of small-angle scattering. *Journal of Applied Crystallography, 42*(2), 347–353. https://doi.org/10.1107/S0021889809002222

Imbs, T. I., & Zvyagintseva, T. N. (2018). Phlorotannins are polyphenolic metabolites of brown algae. *Russian Journal of Marine Biology, 44*(4), 263–273. https://doi.org/10.1134/S106307401804003X

Kantrong, H., Aussanasuwannakul, A., Rodkwan, N., & Chitisankul, W. T. (2024). Effect of mechanical treatment from extrusion process on physicochemical properties of okara cellulose powder. *Scientific Reports, 14*(1), Article 22193. https://doi.org/10.1038/s41598-024-73819-5, 2024 14:1.

Karakuş, M.Ş. (2025). Structural properties, mechanical behavior, and food protecting ability of chickpea protein-derived biopolymer films. *Polymers, 17*(14), 1938. https://doi.org/10.3390/POLYM17141938, 2025, Vol. 17, Page 1938.

Khan, T., Sebaey, T. A., Muthukumar, C., Rao, H. I., Shahroze, R. M., & Parthasarathy, V. (2025). Prediction of the tensile properties of biocomposites: A review of micro-mechanical models. *Biomass Conversion and Biorefinery, 15*(9), 13123–13141. https://doi.org/10.1007/S13399-024-06159-Z/FIGURES/9

Kieffer, J., & Wright, J. P. (2013). PyFAI: A Python library for high performance azimuthal integration on GPU. *Powder Diffraction, 28*(S2), S339–S350. https://doi.org/10.1017/S0885715613000924

Kloareg, B., Badis, Y., Cock, J. M., & Michel, G. (2021). Role and evolution of the extracellular matrix in the acquisition of complex multicellularity in eukaryotes: A macroalgal perspective. *Genes, 12*(7). https://doi.org/10.3390/genes12071059

Klonos, P. A., Evangelopoulou, A., Terzopoulou, Z., Zamboulis, A., Valera, M.Á., Mangas, A., Kyritsis, A., & Bikiaris, D. N. (2022). Revisiting non-conventional crystallinity-induced effects on molecular mobility in sustainable diblock copolymers of Poly(propylene adipate) and polylactide. *Molecules, 27*(21), 7449. https://doi.org/10.3390/MOLECULES27217449, 2022, Vol. 27, Page *7449*.

Krishnan, L., Ravi, N., Kumar Mondal, A., Akter, F., Kumar, M., Ralph, P., & Kuzhiumparambil, U. (2024). Seaweed-based polysaccharides – Review of extraction, characterization, and bioplastic application. *Green Chemistry, 26*(10), 5790–5823. https://doi.org/10.1039/D3GC04009G

Liu, J., Zhang, R., Ci, M., Sui, S., & Zhu, P. (2019). Sodium alginate/cellulose nanocrystal fibers with enhanced mechanical strength prepared by wet spinning. *Journal of Engineered Fibers and Fabrics, 14*. https://doi.org/10.1177/1558925019847553/ASSET/F8FCE016-68FA-4D86-B6F9-70FAC1954467/ASSETS/IMAGES/LARGE/10.1177_1558925019847553-FIG7.JPG

Martínez-Sanz, M., Cebrián-Lloret, V., Mazarro-Ruiz, J., & López-Rubio, A. (2020). Improved performance of less purified cellulosic films obtained from agar waste biomass. *Carbohydrate Polymers, 233*, Article 115887. https://doi.org/10.1016/J.CARBPOL.2020.115887

Martínez-Sanz, M., Fabra, M. J., Gómez-Mascaraque, G., L, & López-Rubio, A. (2018). Structural effects of microalgae additives on the starch gelatinisation process. *Food Hydrocolloids, 77*, 257–269. https://doi.org/10.1016/J.FOODHYD.2017.10.002

Nurhayati, N., Irianto, H. E., Chalid, M., & Riastuti, R. (2025). Morphological and crystallinity studies of Nanofiber cellulose based on sargassum sp. using multistep preparation. *Indonesian Journal of Chemistry, 25*(4), 1156–1166. https://doi.org/10.22146/IJC.104211

O'Brien, R., Hayes, M., Sheldrake, G., Tiwari, B., & Walsh, P. (2022). Macroalgal proteins: A review. *Foods, 11*(4). https://doi.org/10.3390/foods11040571

Park, S., Baker, J. O., Himmel, M. E., Parilla, P. A., & Johnson, D. K. (2010). Cellulose crystallinity index: Measurement techniques and their impact on interpreting cellulase performance. *Biotechnology for Biofuels, 3*(1), 10. https://doi.org/10.1186/1754-6834-3-10/TABLES/2

Pastoriza, S., & Rufián-Henares, J. A. (2014). Contribution of melanoidins to the antioxidant capacity of the Spanish diet. *Food Chemistry, 164*, 438–445. https://doi.org/10.1016/J.FOODCHEM.2014.04.118

Perera, K. Y., Sharma, S., Pradhan, D., Jaiswal, A. K., & Jaiswal, S. (2021). Seaweed polysaccharide in food contact materials (active packaging, intelligent packaging, edible films, and coatings). *Foods, 10*(9). https://doi.org/10.3390/foods10092088

Pérez-Bassart, Z., Martínez-Abad, A., Reyes, A., López-Rubio, A., & Fabra, M. J. (2023). Ultrasound-treatment as a promising strategy to develop biodegradable films

obtained from mushroom waste biomass. *Food Hydrocolloids, 135*, Article 108174. https://doi.org/10.1016/J.FOODHYD.2022.108174

Petcharat, T., Chaijan, M., Indriani, S., Pongsetkul, J., Karnjanapratum, S., & Nalinanon, S. (2025). Modulating fish Gelatin Gelling Properties through furcellaran addition: A structural and physicochemical analysis. *Gels, 11*(6), 381. https://doi.org/10.3390/GELS11060381, 2025, Vol. 11, Page 381.

Plaza, M., Amigo-Benavent, M., del Castillo, M. D., Ibáñez, E., & Herrero, M. (2010). Facts about the formation of new antioxidants in natural samples after subcritical water extraction. *Food Research International, 43*(10), 2341–2348. https://doi.org/10.1016/J.FOODRES.2010.07.036

Re, R., Pellegrini, N., Proteggente, A., Pannala, A., Yang, M., & Rice-Evans, C. (1999). Antioxidant activity applying an improved ABTS radical cation decolorization assay. *Free Radical Biology and Medicine, 26*(9–10), 1231–1237. https://doi.org/10.1016/S0891-5849(98)00315-3

Ross, A. B., Anastasakis, K., Kubacki, M., & Jones, J. M. (2009). Investigation of the pyrolysis behaviour of brown algae before and after pre-treatment using PY-GC/MS and TGA. *Journal of Analytical and Applied Pyrolysis, 85*(1–2), 3–10. https://doi.org/10.1016/J.JAAP.2008.11.004

Saeman, J. F. (1945). Kinetics of Wood Saccharification - Hydrolysis of Cellulose and Decomposition of sugars in Dilute acid at high temperature. *Industrial & Engineering Chemistry, 37*(1), 43–52. https://doi.org/10.1021/ie50421a009

Salem, D. M. S. A., & Ismail, M. M. (2022). Characterization of cellulose and cellulose nanofibers isolated from various seaweed species. *Egyptian Journal of Aquatic Research, 48*(4), 307–313. https://doi.org/10.1016/J.EJAR.2021.11.001

Sanz, V., Baltrusch, K. L., Torres, M. D., Domínguez, H., Fabra, M. J., & López-Rubio, A. (2026). Valorisation of Ulva spp. green seaweed and its residues from pressurized hot water extraction: A comparative study of casting and melt-compounding techniques for film production. *Food Hydrocolloids, 172*, Article 112087. https://doi.org/10.1016/J.FOODHYD.2025.112087

Singh, A. K., Kim, J. Y., & Lee, Y. S. (2022). Phenolic compounds in active packaging and edible Films/Coatings: Natural bioactive molecules and novel packaging ingredients. *Molecules, 27*(21), 7513. https://doi.org/10.3390/MOLECULES27217513, 2022, Vol. 27, Page 7513.

Singleton, V. L., Orthofer, R., & Lamuela-Raventós, R. M. (1999). Analysis of total phenols and other oxidation substrates and antioxidants by means of folin-ciocalteu reagent. *Methods in Enzymology, 299*, 152–178. https://doi.org/10.1016/S0076-6879(99)99017-1

Sirviö, J. A., Kantola, A. M., & Ämmälä, A. (2023). Cellulose nanofibers from nonbleached and hydrogen peroxide bleached acidic thiourea treated sawdust. *Journal of Cleaner Production, 423*, Article 138824. https://doi.org/10.1016/J.JCLEPRO.2023.138824

Starowicz, M., & Zieliński, H. (2019). How maillard reaction influences sensorial properties (Color, flavor and texture) of food products? *Food Reviews International, 35*(8), 707–725. https://doi.org/10.1080/87559129.2019.1600538

Steiner, K., & Florack, A. (2023). The influence of packaging color on consumer perceptions of healthfulness: A systematic review and theoretical framework. *Foods, 12*(21), 3911. https://doi.org/10.3390/FOODS12213911, 2023, Vol. 12, Page 3911.

Tareen, A. K., Punsuvon, V., & Parakulsuksatid, P. (2020). Investigation of alkaline hydrogen peroxide pretreatment to enhance enzymatic hydrolysis and phenolic compounds of oil palm trunk. *3 Biotech, 10*(4), 179. https://doi.org/10.1007/S13205-020-02169-6

Terauchi, M., Nagasato, C., Inoue, A., Ito, T., & Motomura, T. (2016). Distribution of alginate and cellulose and regulatory role of calcium in the cell wall of the brown alga Ectocarpus siliculosus (Ectocarpales, Phaeophyceae). *Planta, 244*(2), 361–377. https://doi.org/10.1007/S00425-016-2516-4/TABLES/1

Thiviya, P., Gamage, A., Liyanapathiranage, A., Makehelwala, M., Dassanayake, R. S., Manamperi, A., Merah, O., Mani, S., Koduru, J. R., & Madhujith, T. (2023). Algal polysaccharides: Structure, preparation and applications in food packaging. *Food Chemistry, 405*, Article 134903. https://doi.org/10.1016/J.FOODCHEM.2022.134903

Uranga, J., Carranza, T., Peñalba, M., de la Caba, K., & Guerrero, P. (2023). Valorization of agar production residue as a filler in soy protein hydrogels for 3D printing. *International Journal of Bioprinting, 9*(4), 731. https://doi.org/10.18063/IJB.731

Valério Filho, A., Santana, L. R., Motta, N. G., Passos, L. F., Wolke, S. lnes, Mansilla, A., Astorga-España, M. S., Becker, E. M., de Pereira, C. M. P., & Carreno, N. L. V. (2023). Extraction of fatty acids and cellulose from the biomass of algae Durvillaea Antarctica and Ulva lactuca: An alternative for biorefineries. *Algal Research, 71*, Article 103084. https://doi.org/10.1016/J.ALGAL.2023.103084

Vega-Gómez, L. M., Molina-Gilarranz, I., Fontes-Candia, C., Cebrián-Lloret, V., Recio, I., & Martínez-Sanz, M. (2024). Production of hybrid protein-polysaccharide extracts from Ulva spp. seaweed with potential as food ingredients. *Food Hydrocolloids, 153*, Article 110046. https://doi.org/10.1016/J.FOODHYD.2024.110046

Vega-Gómez, L. M., Torrego-Moreno, E., Cebrián-Lloret, V., Castanedo, M., Martínez, J. C., Recio, I., & Martínez-Sanz, M. (2026). Unravelling the multi-scale structure of cell walls from edible seaweed species and the impact of processing treatments. *Food Hydrocolloids, 170*, Article 111720. https://doi.org/10.1016/J.FOODHYD.2025.111720

Wang, J., Minami, E., & Kawamoto, H. (2020). Thermal reactivity of hemicellulose and cellulose in cedar and beech wood cell walls. *Journal of Wood Science, 66*(1), 41. https://doi.org/10.1186/S10086-020-01888-X/FIGURES/9

Wang, T., & Hong, M. (2016). Solid-state NMR investigations of cellulose structure and interactions with matrix polysaccharides in plant primary cell walls. *Journal of Experimental Botany, 67*(2), 503–514. https://doi.org/10.1093/JXB/ERV416

Willför, S., Pranovich, A., Tamminen, T., Puls, J., Laine, C., Suurnäkki, A., Saake, B., Uotila, K., Simolin, H., Hemming, J., & Holmbom, B. (2009). Carbohydrate analysis of plant materials with uronic acid-containing polysaccharides–A comparison between different hydrolysis and subsequent chromatographic analytical techniques. *Industrial Crops and Products, 29*(2–3), 571–580. https://doi.org/10.1016/J.INDCROP.2008.11.003

Wilpiszewska, K., Antosik, A. K., Schmidt, B., Janik, J., & Rokicka, J. (2020). Hydrophilic films based on carboxymethylated derivatives of starch and cellulose. *Polymers, 12*(11), 2447. https://doi.org/10.3390/POLYM12112447, 2020, Vol. 12, P*age 2447*.

Xiao, M., Shawkey, M. D., Dhinojwala, A., Xiao, M., Dhinojwala, A., Xiao John Paulson, M. A., & Shawkey, M. D. (2020). Bioinspired melanin-based optically active materials. *Advanced Optical Materials, 8*(19), Article 2000932. https://doi.org/10.1002/ADOM.202000932

Yaich, H., Amira, A. B., Abbes, F., Bouaziz, M., Besbes, S., Richel, A., Blecker, C., Attia, H., & Garna, H. (2017). Effect of extraction procedures on structural, thermal and antioxidant properties of ulvan from Ulva lactuca collected in Monastir coast. *International Journal of Biological Macromolecules, 105*, 1430–1439. https://doi.org/10.1016/J.IJBIOMAC.2017.07.141

Yao, W., Yong, J., Lv, B., Guo, S., You, L., Cheung, P. C. K., & Kulikouskaya, V. I. (2023). Enhanced in vitro anti-photoaging effect of degraded seaweed polysaccharides by UV/H2O2 treatment. *Marine Drugs, 21*(8), 430. https://doi.org/10.3390/MD21080430, 2023, Vol. 21, Page 430.